



The Swift Deep Galactic Plane Survey (DGPS) Phase I Catalog

B. O'Connor^{1,2,3}, C. Kouveliotou¹, P. A. Evans⁴, N. Gorgone¹, A. J. van Kooten¹, S. Gagnon¹, H. Yang¹,
M. G. Baring⁵, E. Bellm⁶, P. Beniamini^{1,7,8}, J. Brink^{9,10}, D. A. H. Buckley^{9,10,11,12}, S. B. Cenko^{3,13},
O. D. Egbo^{9,14}, E. Göğüş¹⁵, J. Granot^{1,7,8}, C. Hailey¹⁶, J. Hare^{3,17,18}, F. Harrison¹⁹, D. Hartmann²⁰,
A. J. van der Horst¹, D. Huppenkothen²¹, L. Kaper²², O. Kargaltsev¹, J. A. Kennea²³, K. Mukai^{24,25}, P. O. Slane²⁶,
D. Stern²⁷, E. Troja²⁸, Z. Wadiasingh^{2,3,17}, R. A. M. J. Wijers^{1,29}, P. Woudt⁹, and G. Younes^{1,3}

¹Department of Physics, The George Washington University, Washington, DC 20052, USA; oonorb@gwmail.gwu.edu

²Department of Astronomy, University of Maryland, College Park, MD 20742-4111, USA

³Astrophysics Science Division, NASA Goddard Space Flight Center, 8800 Greenbelt Road, Greenbelt, MD 20771, USA

⁴School of Physics and Astronomy, University of Leicester, University Road, Leicester, LE1 7RH, UK

⁵Department of Physics and Astronomy—MS 108, Rice University, 6100 Main Street, Houston, TX 77251-1892, USA

⁶DIRAC Institute, Department of Astronomy, University of Washington, 3910 15th Avenue NE, Seattle, WA 98195, USA

⁷Department of Natural Sciences, The Open University of Israel, P.O. Box 808, Ra'anana 4353701, Israel

⁸Astrophysics Research Center of the Open University (ARCO), The Open University of Israel, P.O. Box 808, Ra'anana 4353701, Israel

⁹Department of Astronomy, University of Cape Town, Private Bag X3, Rondebosch 7701, South Africa

¹⁰South African Astronomical Observatory, P.O. Box 9, Observatory 7935, Cape Town, South Africa

¹¹Southern African Large Telescope, P.O. Box 9, Observatory 7935, Cape Town, South Africa

¹²Department of Physics, University of the Free State, P.O. Box 339, Bloemfontein 9300, South Africa

¹³Joint Space-Science Institute, University of Maryland, College Park, MD 20742 USA

¹⁴South African Astronomical Observatory, P.O. Box 9, 7935 Observatory, South Africa

¹⁵Sabancı University, Faculty of Engineering and Natural Sciences, İstanbul 34956 Turkey

¹⁶Columbia Astrophysics Laboratory, Columbia University, New York, NY 10027, USA

¹⁷Center for Research and Exploration in Space Science and Technology, NASA/GSFC, Greenbelt, MD 20771, USA

¹⁸The Catholic University of America, 620 Michigan Avenue NE, Washington, DC 20064, USA

¹⁹Cahill Center for Astrophysics, California Institute of Technology, 1216 East California Boulevard, Pasadena, CA 91125, USA

²⁰Department of Physics and Astronomy, Clemson University, Kinard Lab of Physics, Clemson, SC 29634-0978, USA

²¹SRON Netherlands Institute for Space Research, Niels Bohrweg 4, 2333CA Leiden, The Netherlands

²²University of Amsterdam, Science Park 904, 1098 XH Amsterdam, The Netherlands

²³Department of Astronomy and Astrophysics, The Pennsylvania State University, 525 Davey Lab, University Park, PA 16802, USA

²⁴CRESST II and X-ray Astrophysics Laboratory, NASA/GSFC, Greenbelt, MD 20771, USA

²⁵Department of Physics, University of Maryland Baltimore County, 1000 Hilltop Circle, Baltimore MD 21250, USA

²⁶Center for Astrophysics, Harvard & Smithsonian, 60 Garden Street, Cambridge, MA 02138, USA

²⁷Jet Propulsion Laboratory, California Institute of Technology, 4800 Oak Grove Drive, Mail Stop 169-221, Pasadena, CA 91109, USA

²⁸University of Rome Tor Vergata, Department of Physics, via della Ricerca Scientifica 1, I-00100, Rome, IT, Italy

²⁹Anton Pannekoek Institute, University of Amsterdam, Postbus 94249, 1090 GE Amsterdam, The Netherlands

Received 2023 June 25; revised 2023 September 20; accepted 2023 September 21; published 2023 November 28

Abstract

The Swift Deep Galactic Plane Survey (DGPS) is a Swift Key Project consisting of 380 tiled pointings covering $\sim 40 \text{ deg}^2$ of the Galactic plane between longitude $10 < |l| < 30 \text{ deg}$ and latitude $|b| < 0.5 \text{ deg}$. Each pointing has a 5 ks exposure, yielding a total of 1.9 Ms spread across the entire survey footprint. Phase I observations were carried out between 2017 March and 2021 May. The survey is complete to depth $L_X > 10^{34} \text{ erg s}^{-1}$ to the edge of the Galaxy. The main survey goal is to produce a rich sample of new X-ray sources and transients, while also covering a broad discovery space. Here, we introduce the survey strategy and present a catalog of sources detected during Phase I observations. In total, we identify 928 X-ray sources, of which 348 are unique to our X-ray catalog. We report on the characteristics of sources in our catalog and highlight sources newly classified and published by the DGPS team.

Unified Astronomy Thesaurus concepts: X-ray astronomy (1810); Surveys (1671); Catalogs (205); X-ray binary stars (1811)

Supporting material: machine-readable tables

1. Introduction

Since the inception and discovery of X-ray astronomy, from the detection of Sco X-1 and the launch of the first X-ray satellite in 1970 (Uhuru; Giacconi et al. 1971), a diverse assortment of X-ray-emitting sources have been discovered and sorted into numerous distinct classes. These classes include chromospheric activity from young stars, cataclysmic variables (CVs), symbiotic binaries, young

stellar objects (YSOs), magnetars, and X-ray binaries comprising a compact object, either a neutron star (NS) or black hole, and a low-mass (LMXBs) or high-mass (HMXBs) star.

Within our Galaxy, the brightest X-ray sources are known to be X-ray binaries with peak X-ray luminosities in excess of $L_X > 10^{36-39} \text{ erg s}^{-1}$. However, our Milky Way also hosts a significant population of faint X-ray sources ($L_X < 10^{33-35} \text{ erg s}^{-1}$) (Muno et al. 2005a, 2005b; Degenaar & Wijnands 2009, 2010). These sources are likely dominated by magnetic CVs (Barrett et al. 1999; Wang et al. 2002; Revnivtsev et al. 2009; Pretorius et al. 2013), quiescent LMXBs (Muno et al. 2005a, 2005b), and quiescent magnetars (Coti Zelati et al. 2018), among others. Their

discovery is crucial to expand our understanding of their source populations and their formation pathways within our Galaxy.

X-ray surveys of the Galactic Plane (GP) present a prime opportunity for discovery of these faint sources. Thus far, sensitive and high-resolution X-ray satellites, such as XMM-Newton or Chandra (Wijnands et al. 2006; Jonker et al. 2011; Nebot Gómez-Morán et al. 2013), have been used to search for serendipitous faint X-ray sources within the true target’s field of view. Such procedures, however, are not uniform in depth nor do they cover the full extent of the GP, relying instead on pointings directed at known bright sources. Therefore, dedicated, homogeneous X-ray surveys are required to identify the population and number of faint X-ray sources within the Galaxy.

The Neil Gehrels Swift Observatory (Gehrels et al. 2004) X-ray Telescope (XRT; Burrows et al. 2005) utilizes a CCD detector with sensitivity to X-ray photons over the range 0.3–10 keV. The instrument field of view (FOV) is $23'6 \times 23'6$ with an effective area of 110 cm^2 at 1.5 keV and an angular resolution of $18''$. The low background ($10^{-6} \text{ counts s}^{-1} \text{ pix}^{-1}$; Evans et al. 2014), arcsecond source localization, and fast slew rate make the Swift/XRT optimal for surveys of crowded environments, such as the GP (Reynolds et al. 2013), Small Magellanic Cloud (Kennea et al. 2018), and the Galactic bulge (Shaw et al. 2020; Bahramian et al. 2021).

Here, we outline our Swift Deep Galactic Plane Survey (DGPS) strategy and present the catalog of sources detected in Phase I observations across the $\sim 40 \text{ deg}^2$ portion of the GP covered by the DGPS. We present the survey design and strategy in Section 2. In Section 3, we discuss our source detection procedures and the process for creating a unique source catalog. The catalog results, discussion of implications, and overall conclusions are presented in Sections 4, 5, and 6, respectively.

2. Survey Footprint and Observing Strategy

The Swift Deep Galactic Plane Survey (PI: C. Kouveliotou) is a Swift Key Project and NuSTAR Legacy Program³⁰ covering $\sim 40 \text{ deg}^2$ of the GP (Figure 1) between Galactic longitude $10 < |l| < 30 \text{ deg}$ and latitude $|b| < 0.5 \text{ deg}$. The total sky coverage of the survey is 36 deg^2 when correcting for tile overlaps and the shape of the XRT FOV. The survey encompasses 380 unique XRT pointings (see Figures 2 and 3), each observed for $\sim 5 \text{ ks}$ for a total of $\sim 1.93 \text{ Ms}$ exposure carried out between 2017 March to 2021 May. Approximately half of these observations were performed between 2017 and 2019, and the second half between 2020 and 2021. All observations were performed with the Swift X-ray Telescope (XRT; Burrows et al. 2005) in photon-counting mode.

The design of our survey (latitude and longitude range; Figures 2 and 3) was driven by our primary science goal of thoroughly characterizing the magnetar and HMXB populations in the Milky Way by their persistent emission, while avoiding the crowded Galactic center (Figure 1). We have additionally selected the survey footprint such that each tile has a $4'$ overlap with its neighbor, taking into account the $23'6$ XRT FOV.

In total, the survey comprises 769 observations,³¹ with Swift covering the 380 pointings (Figure 2), including those observed

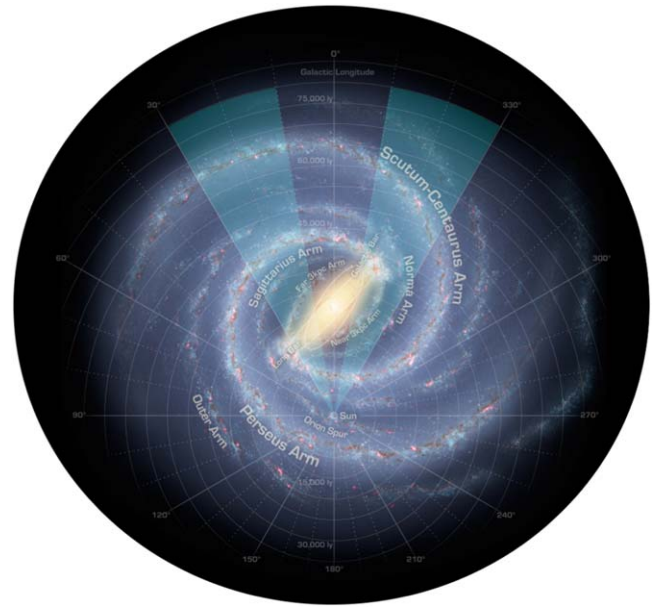


Figure 1. The shaded blue regions show the line of sight of the DGPS footprint through the Milky Way’s disk. The background image is an illustration of the Milky Way, with credit to NASA/JPLCaltech/ESO/R. Hurt.

during the DGPS Pilot Survey. This is due to the fact that, in most cases ($\sim 70\%$), multiple observations of the same field were required to yield a total of 5 ks exposure. In Figure 4, we display a histogram of exposure times for these 769 single-epoch observations. We note that, although a significant fraction (47%) of single-epoch observations consisted of less than 2 ks of exposure, the median cumulative exposure across the survey footprint is 4.6 ks (Figures 2 and 4). The fact that many tiles were observed multiple times was extremely useful for the identification of variable X-ray sources (see Sections 4.3 and 5.4).

On average, the survey is complete (Section 5.1) to a depth of $L_X > 1.0 \times 10^{34} \text{ erg s}^{-1}$, to the edge of the Galaxy. However, it affords source detection to limits of $L_X \sim 1.0 \times 10^{33} \text{ erg s}^{-1}$ out to $\sim 3\text{--}6 \text{ kpc}$.

3. Swift/XRT Data Analysis

Here, we outline our process for analyzing all 769 DGPS observations. Due to the long-term nature of the project, and the need for XRT to return to the same field multiple times (Figure 4), we performed an initial analysis of all data when it was first obtained (Section 3.1). After the end of Phase I observations, we performed a final processing (Section 3.2) of all observations to create the DGPS Phase I catalog.

To do this, we performed source detection on mosaics of the DGPS observations (Section 2). Following the creation of a unique source catalog, we pulled additional information (e.g., flux, hardness ratio (HR), and variability) from the Living Swift-XRT Point-source catalog³² (LSXPS; Evans et al. 2023). LSXPS has processed all Swift/XRT observations, including those comprising the DGPS, and this step avoids redundancy in reprocessing all of the data and increases the overall scientific impact by allowing us to have an improved grasp on the source characteristics.

³⁰ <https://www.nustar.caltech.edu/page/59#g9>

³¹ An observation is defined as all exposures covering a specific pointing obtained within a single UT day.

³² <https://swift.ac.uk/LSXPS/docs.php>

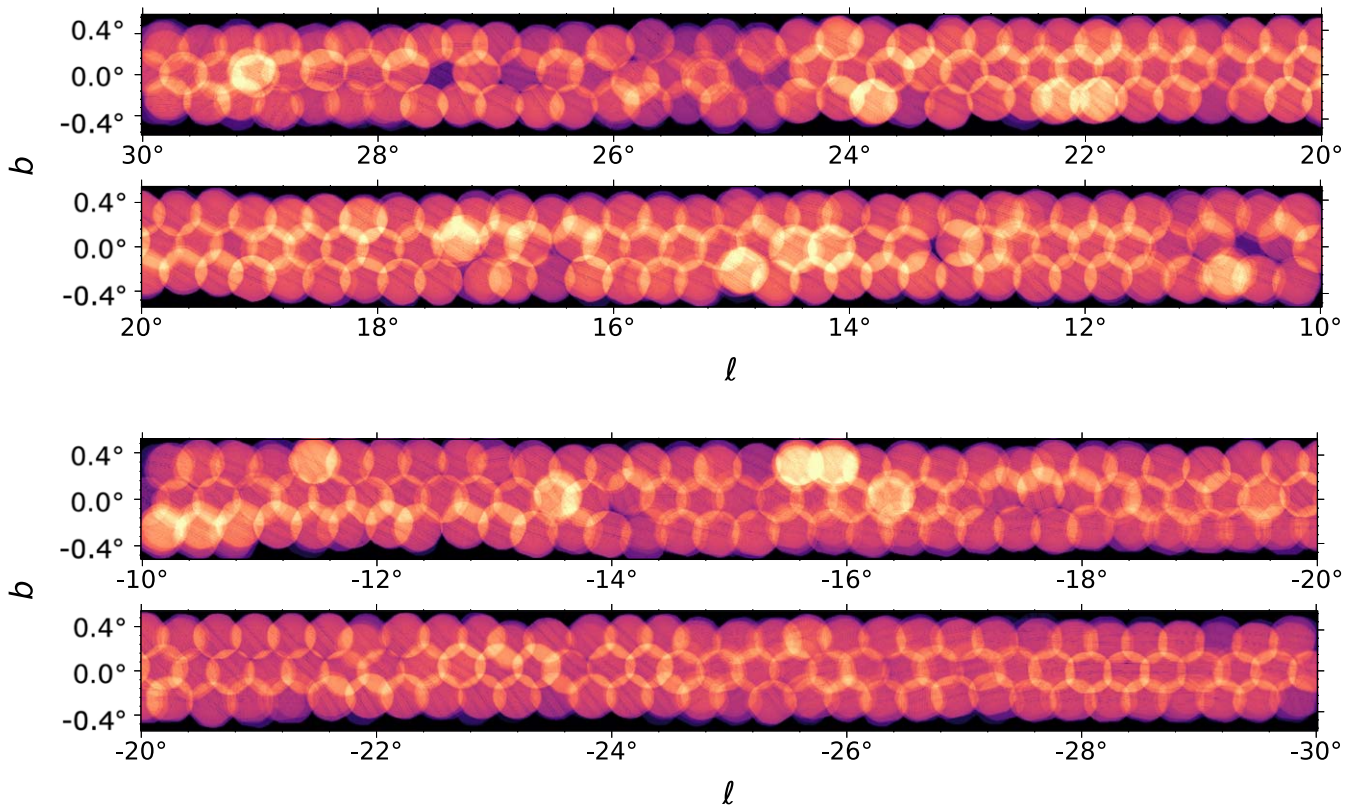


Figure 2. Swift/XRT exposure map of the DGPS footprint. The $4'$ overlap region between adjacent tiles is clearly demonstrated. A few tile positions were serendipitously observed twice, leading to a higher exposure (brighter regions). The median exposure across all pixels is 4.6 ks. The variation in exposure in the two observed regions of the GP is negligible.

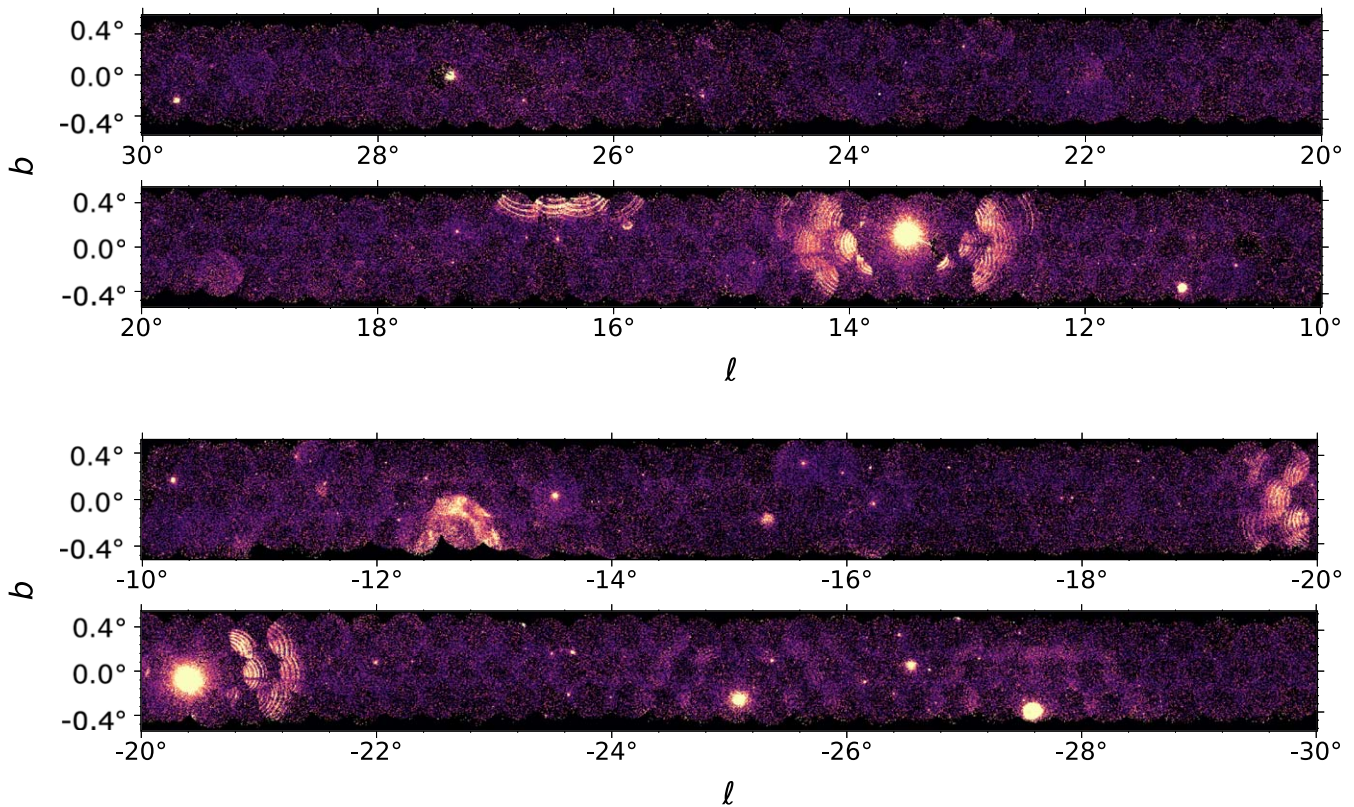


Figure 3. Full XRT band (0.3–10 keV) mosaic of the Galactic plane using an Aitoff projection in Galactic coordinates. The image covers the full footprint of DGPS Phase I. The pixel size is $4''.7 \text{ pix}^{-1}$, and images have been smoothed with a Gaussian kernel (with FWHM of 3 pixels) to improve visual clarity. The image has been divided by the exposure map (Figure 2) in order to smooth out exposure-related background in the overlapping regions. The dominant sources of stray light at $l \approx -25^\circ$, $-20^\circ 5$, and $13^\circ 5$ are the LMXBs 4U 1624-49, 4U 1642-45, and GX 13+01.

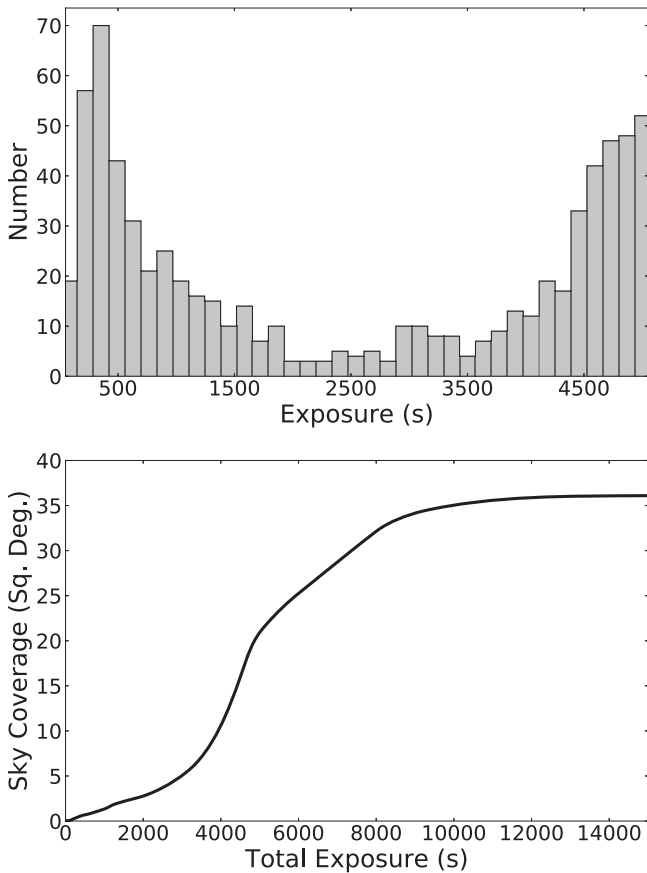


Figure 4. Top: histogram of single-epoch Swift/XRT exposure time for all DGPS observations. Bottom: sky coverage as a cumulative function of the exposure time (corrected for vignetting and bad pixels) across the entire DGPS footprint after mosaicing all observations. The total sky coverage of the survey is 36 deg^2 . The median exposure time is 4.6 ks. The overlap regions between tiles lead to a higher exposure of up to 15–20 ks.

Through this process, we discovered that there exists a subset of DGPS sources ($\sim 14\%$) that are not in the LSXPS catalog (Section 3.2.1). These sources lack some of the additional information that comes from LSXPS (e.g., HR variability), and we discuss their significance further in Sections 3.2.1 and 4.1.1. All sources detected by DGPS in our analysis of the mosaics (e.g., Figure 5), including those not found in LSXPS, are incorporated into our full catalog (see also Appendix 5.3), and this includes those sources that were not identified in LSXPS processing (Evans et al. 2023).

3.1. Quick-look Analysis

The identification and prompt follow-up of variable or transient sources detected as part of the survey required a rapid analysis of quick-look data³³ as these became available ~ 2 – 6 hr after the observations. Quick-look data are not the final fully processed data, and are instead treated as a preliminary first look in order to identify sources displaying variability on a shorter timescale than the fully processed data are available (~ 1 – 2 weeks after the quick-look data.³⁴) The former data, however, allowed for rapid multiwavelength follow-up observations. The single-epoch quick-look data were initially processed within a day of each XRT observation.

³³ <https://www.swift.ac.uk/archive/ql.php>

³⁴ https://swift.gsfc.nasa.gov/quick-look/swift_process_overview.html

In many cases ($\sim 70\%$), Swift did not perform the full ~ 5 ks exposure in a single epoch (see Figure 4). Therefore, in order to reach the full exposure for each tile, Swift carried out multiple observations,³⁵ sometimes taken months apart. We utilized this to better identify variability by comparing the source flux between each observation. We additionally checked archival flux values from available X-ray catalogs. We selected previously unknown or unclassified variable sources with an unabsorbed X-ray flux brighter than $F_X > 1.0 \times 10^{-12} \text{ erg cm}^{-2} \text{ s}^{-1}$ (0.3–10 keV) for Target of Opportunity (ToO) follow-up with a variety of X-ray satellites, such as XMM-Newton, Chandra, NuSTAR, and NICER, through our approved programs; see, e.g., Gorgone et al. (2019, 2021), O'Connor et al. (2022, 2023a, 2023b).

3.2. Final Image Processing and Source Detection

The rapid quick-look analysis of DGPS observations does not reach the full depth of the survey. In order to produce a complete source catalog, we turned toward a more robust, yet computationally intensive, data analysis pipeline used to generate previous Swift X-ray catalogs (Evans et al. 2014, 2020). This pipeline allows for the mosaicing of all observations within the DGPS. However, the Swift DGPS covers $\sim 40 \text{ deg}^2$ of the Galactic plane, and performing source detection on regions of this size is infeasible due to the computational cost. Therefore, in order to reduce the computation time, while still achieving the maximum exposure across every part of the survey, we defined 124 small mosaics covering the entire Phase I survey area. The mosaics were created such that there is an overlap for every mosaic, which means that some pointings were part of multiple mosaics. This ensures that every possible overlap of tiles is accounted for, and it allowed us to obtain the maximum exposure at every location within the DGPS footprint. An example mosaic is displayed in Figure 5.

The image processing, mosaic creation, and source detection algorithm are described in detail in Evans et al. (2014, 2020). The pipeline made use of HEASoFT 6.29. The iterative source detection procedure classifies each source using numerous quality flags, such as “good,” “reasonable,” or “poor” (see Evans et al. 2014, 2020 for details).³⁶ These flags indicate the level of significance of the detection, and they were calibrated using simulations of point sources. The false-positive rate for *good* sources is 0.3%, and it increases to 1% when also including *reasonable* sources, whereas including *poor* sources yields a rate of spurious sources on the order of 10% (Evans et al. 2020). These false-positive rates are considered cumulative, and we note that the actual false-positive rates for *reasonable* and *poor* sources are $\sim 7\%$ and $\sim 35\%$, respectively. Therefore, we remove sources with a *poor* quality flag.

The Evans et al. (2020) pipeline also includes quality flags to prevent spurious sources in regions contaminated by stray light or extended sources (e.g., supernova remnants) as well as sources that are possible aliases of bright sources (see Table 5 of Evans et al. 2014). We have excluded all sources occurring in the point-spread function (PSF) of extremely bright sources, in regions of stray light or known extended objects, as well as

³⁵ In most cases, it took Swift three observations of varying length for an individual tile to reach 5 ks exposure.

³⁶ <https://swift.ac.uk/2SXPS/docs.php>

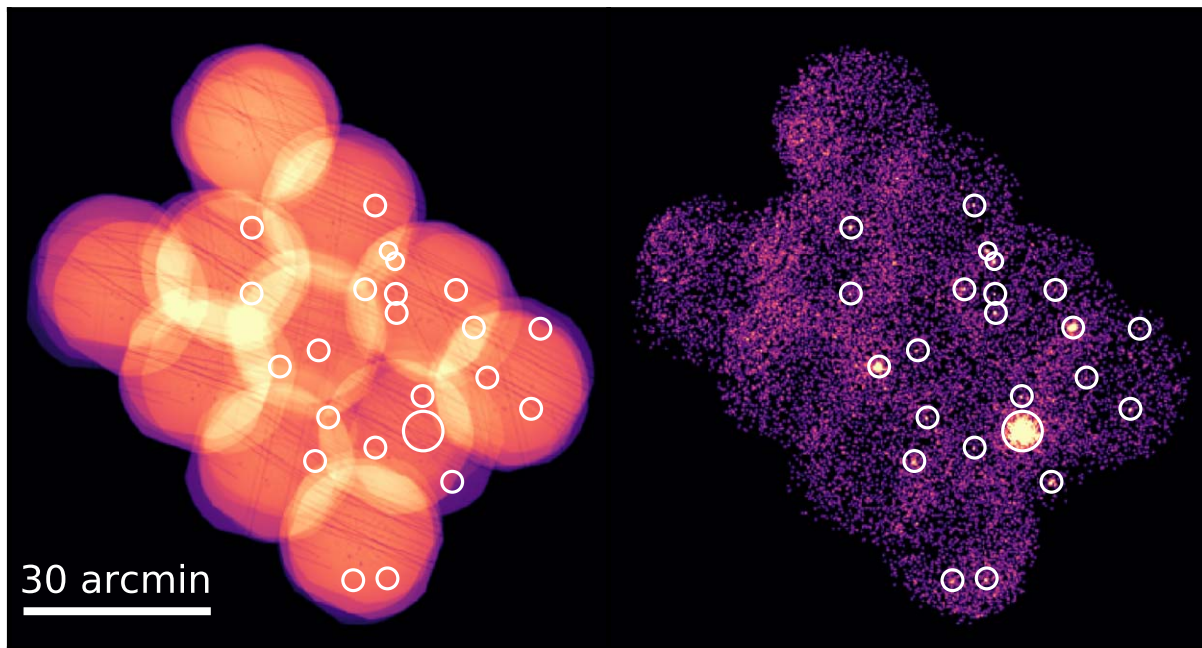


Figure 5. Example exposure map and science image (0.3–10 keV) of a DGPS mosaic. The mosaic is centered at $l, b = 333^\circ 87, 0^\circ 026$. White circles represent the locations of sources detected in this image. The bright source to the right of the image is MAXI J1651-501, a Type-I X-ray burster uncovered through DGPS observations (Gorgone et al. 2019). A weak stray light pattern (concentric bands) is visible on the left end of the mosaic. The images have been rebinned ($7'' 07 \text{ pix}^{-1}$) and smoothed with a Gaussian kernel (with FWHM of 3 pixels) for display purposes.

those due to optical loading.³⁷ The field flags were set manually by Evans et al. (2020).

After removing all sources with quality flags, we began by merging all blindly detected sources in the same mosaic across the different energy bands. Source detection is run independently in four energy bands³⁸: the soft band (SB; 0.3–1 keV), medium band (MB; 1–2 keV), hard band (HB; 2–10 keV), and full band (FB; 0.3–10 keV). We merged sources that were identified as the same source, but in different energy bands, by defining a match as either being within 10 pixels (1 pixel = $2'' 36$) or consistent at the 99.7% level using Rayleigh statistics. At this stage, we include only the statistical position errors, as each source within a single mosaic has the same astrometric solution. This process yields a list of unique sources identified in each mosaic.

As there is a one-tile overlap between each mosaic, there are some duplicate sources that must be removed. We therefore crossmatched the source lists between every mosaic in order to remove duplicate sources that were consistent at the 99.7% confidence level (including both the statistical and systematic error on the source positions). We are then left with a unique list of sources detected across the entire DGPS footprint.

The source count rates and fluxes in each energy band were then pulled from LSXPS using the API tool.³⁹ We determined the LSXPS counterpart to each DGPS source using a radius of $20''$ or the 99.7% combined error radius. As the LSXPS is a low-latency, continuously updated catalog, we note that our crossmatch was performed on the LSXPS catalog of 2022 August 31. We also note that we only include sources in

LSXPS that are detected in our DGPS mosaics, and therefore only sources to the completeness limits of the DGPS.

The count rates were converted to a 0.3–10 keV flux assuming a power-law spectrum with photon index $\Gamma = 1.7$ and the Galactic hydrogen column density in the source direction from Willingale et al. (2013). We further took from the LSXPS catalog the hardness ratios $HR_1 = M - S/M + S$, $HR_2 = H - M/H + M$, and the Pearson’s χ^2 probability that each source is variable based on their LSXPS lightcurves binned by observation.

The source positions in LSXPS are based on either standard or astrometric positions. We therefore used the API tool to build XRT enhanced positions (Goat et al. 2007; Evans et al. 2009) for all DGPS sources. We successfully built enhanced positions for 290 sources, and we accepted the position with the smallest error. We used the final source positions to name DGPS sources in the format: “DGPS JHHMMSS. $S \pm$ DDMMSS.”

All sources and their properties (along with LSXPS ID; Evans et al. 2023) are displayed in Table 2.⁴⁰ We detected a total of 802 sources, of which 784 are detected in the FB, 724 in the HB, 668 in the MB, and 564 in the SB.

3.2.1. Sources with No LSXPS Counterpart

In addition to those sources described above, we detect ~ 200 sources in the DGPS mosaics that do not have LSXPS counterparts within $60''$ (Evans et al. 2023). We refer to these as non-LSXPS sources throughout the manuscript. There are a number of plausible reasons as to why these sources would not have been detected in the LSXPS mosaics, including a different combination of observations used to build the mosaics in

³⁷ https://swift.ac.uk/analysis/xrt/optical_loading.php

³⁸ The same energy bands were previously used in the 1SXPS, 2SXPS, and LSXPS catalogs (Evans et al. 2014, 2020, 2023).

³⁹ <https://swift.ac.uk/API/>

⁴⁰ Table 2 is available in electronic form at the CDS via anonymous ftp to cdsarc.u-strasbg.fr (130.79.125.5) or via <http://cdsweb.u-strasbg.fr/cgi-bin/qcat?I/ApJS/>.

LSXPS, hot pixels, which are harder to detect in stacked observations, or a lower background to variable or transient sources in the DGPS mosaics, as they include less overall observations. Therefore, there is no obvious reason to exclude these sources from our catalog.

After removing sources with field flags or those lying in the PSF of a bright source, we are left with 126 sources, 83 classified as *good* and 43 as *reasonable*. Based on simulations of Swift/XRT point sources (Evans et al. 2014, 2020), these sources are detected at the 99% confidence level.

We utilized the Python API tool to call the Swift-XRT LSXPS Upper Limit Server⁴¹ (Evans et al. 2023), which allows for the calculation of 3σ upper limits for any position within the LSXPS footprint. We specifically called only the DGPS observations covering the position of each source. Aperture photometry using a circular region with a radius of 12 pixels ($28''$) was then performed on the images in order to determine the source and background counts in each energy band. We then applied the Bayesian procedure of Kraft et al. (1991) to determine whether the source is detected at the 3σ level, and if detected, the mean number of counts and 1σ errors. The Upper Limit Server also computes a PSF correction to account for vignetting and the encircled energy fraction of the circular aperture. After multiplying the number of counts by this correction factor and dividing by the exposure time, we obtain a count rate in each energy band. This is all done through the `mergeUpperLimits` tool. These methods are identical to those utilized to compute count rates for LSXPS sources.

However, we only find a 3σ detection for 35 out of 126 sources with 22 detections in the FB, 17 in the HB, 9 in the MB, and 6 in the SB. Of the 35 sources, 16 were detected in multiple bands using this method. This serves to confirm that at least some of these sources, likely more than 35, are not spurious in nature. We note that the Evans et al. (2020) source detection algorithm does not necessarily require a 3σ statistical significance for detection, and in fact, the signal-to-noise ratio for many of these sources is ~ 2 . Instead, the algorithm computes a likelihood that the source is real, which was calibrated using simulations (Evans et al. 2014, 2020). This could explain why only 35 of 126 sources are above the 3σ threshold according to Kraft et al. (1991).

We convert the count rate to an unabsorbed flux (0.3–10 keV) for each source assuming the median ECF for all DGPS sources detected in LSXPS (Section 3.2). This is dependent on the energy band, and we find median values of $ECF_{FB} = 2.7 \times 10^{-11} \text{ erg cm}^{-2} \text{ counts}^{-1}$ for the full band, and $ECF_{SB} = 5.2 \times 10^{-11} \text{ erg cm}^{-2} \text{ counts}^{-1}$, $ECF_{MB} = 6.6 \times 10^{-11} \text{ erg cm}^{-2} \text{ counts}^{-1}$, and $ECF_{HB} = 4.5 \times 10^{-11} \text{ erg cm}^{-2} \text{ counts}^{-1}$. These ECFs were all determined assuming a power-law X-ray spectrum with photon index $\Gamma = 1.7$ and Galactic hydrogen column density (Willingale et al. 2013).

For these non-LSXPS sources, we record only the standard position derived by the source detection algorithm as performed on the DGPS mosaics. We note that these sources have no multi-epoch (i.e., variability) information, as they are only detected in stacked observations (mosaics). Furthermore, due to their faintness and low number of photons, the hardness ratio information is limited, and instead we record clearly the bandpass in which the source is detected. Due to these limitations, we record the non-LSXPS sources in a separate

table from those with additional LSXPS information. We report the results for these 126 sources in Table 3.⁴² We emphasize that these sources, in addition to those in Table 2, comprise the full DGPS Phase I catalog.

4. Results

4.1. Crossmatching with External Catalogs

We crossmatched the 802 sources in Table 2 with a variety of radio, optical, infrared, and X-ray catalogs in order to identify their multiwavelength counterparts. We defined a match as when the catalog and DGPS positions were consistent at the 99.7% confidence level⁴³ when adding both catalog and DGPS errors in quadrature. The distributions of the 90% position errors are shown in Figure 6 (top panel). The median 90% position error is $4''.6$, leading to a 99.7% error of $\sim 7''$.

We began by searching the SIMBAD astronomical database (Wenger et al. 2000) in order to identify any previous source classifications. As the SIMBAD database does not include positional errors uniformly, it is possible some real associations were missed. For all other catalogs, we include the catalog's positional error added to the DGPS position error in quadrature.

We used `astroquery` (Ginsburg et al. 2019) to search the VizieR database (Ochsenbein et al. 2000) for the following X-ray catalogs: the Chandra Source Catalog (CSC; Evans et al. 2010) Release 2.0, the XMM-Newton Serendipitous Source Catalog (4XMM-DR9; Webb et al. 2020; Traulsen et al. 2020), 1SXPS (Evans et al. 2014), and 2SXPS (Evans et al. 2020), 1SWXRT (D'Elia et al. 2013). In addition to the number of matches in each X-ray catalog, we report the number of unique, previously unknown, X-ray sources. We additionally searched the following optical, infrared, and radio catalogs: USNO-B1 (Monet et al. 2003), Gaia EDR3 (Gaia Collaboration et al. 2021), the Two Micron All Sky Survey (2MASS; Skrutskie et al. 2006), and the Very Large Array Sky Survey (VLASS; Lacy et al. 2020). The results of our crossmatching analysis are displayed in Table 1.

We find that 249 (31%) of DGPS sources were previously unknown to other X-ray surveys (with the exception of LSXPS). In Table 2, we record whether a source has a known X-ray counterpart. Figure 6 (bottom panel) shows the distribution of offsets between X-ray source matches normalized by the 68% position uncertainty of both sources added in quadrature. The distribution of position-error-normalized offsets approximately follows a Rayleigh distribution with scale parameter $\sigma = 1$. However, there is some excess at $R/\sigma > 3$ that may hint at an additional systematic position error that was not included. We note that counterparts in 2SXPS are not included in this calculation, as their separations are tighter than a Rayleigh distribution, due to the use of a similar source detection algorithm on similar data, i.e., the first half of the DGPS data obtained between 2017 and 2019 are included in the 2SXPS catalog. This leads to a bias toward the same centroid location for counterparts in 2SXPS, whereas there is no overlap with 1SWXRT—and therefore no bias against a Rayleigh distribution.

⁴² Table 3 is available in electronic form at the CDS via anonymous ftp to cdsarc.u-strasbg.fr (130.79.125.5) or via <http://cdsweb.u-strasbg.fr/cgi-bin/qcat?J/ApJS/>.

⁴³ In order to convert between the 90% and 99.7% position error, we have assumed that our source position errors follow Rayleigh statistics (Evans et al. 2014, 2020).

⁴¹ <https://swift.ac.uk/LSXPS/ulserv.php>

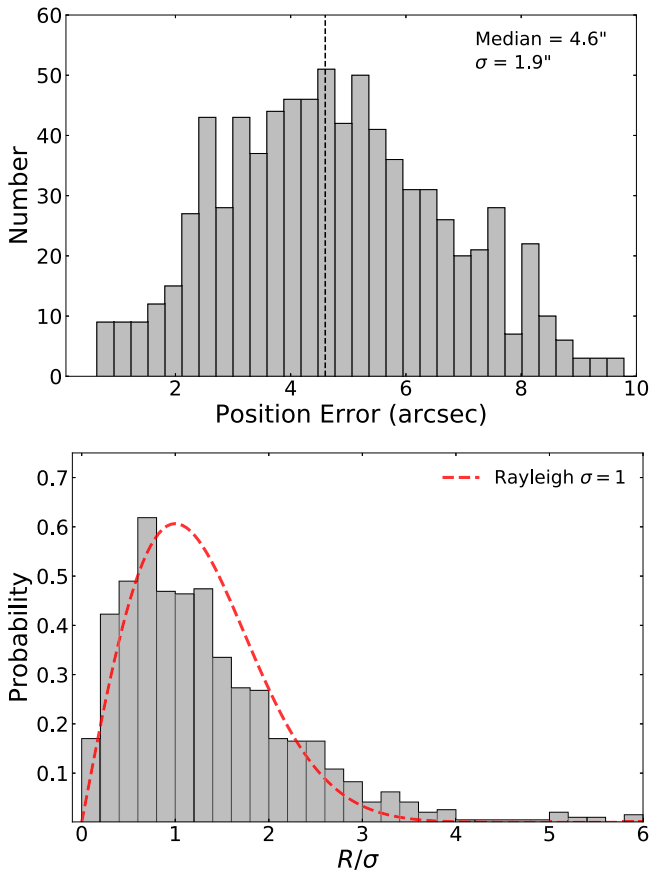


Figure 6. Top: histogram of the 90% X-ray position error for sources in the DGPS catalog. Bottom: radial separation R divided by the 68% error of the DGPS sources and the 68% error of other X-ray source error added in quadrature. The radial separation is from the DGPS source to the X-ray counterpart centroid from 4XMM, 2CSC, and 1SWXRT. The dashed red line shows the expected Rayleigh distribution with $\sigma = 1$.

We determined the number of false associations by shifting all DGPS sources randomly by $1'-2'$ and repeating the crossmatch. All matches found after shifting are considered false positives. We repeated this procedure multiple times. Due to the high density of optical and infrared sources in the crowded GP, generally there are multiple counterparts within a typical X-ray localization (e.g., between two and four Gaia counterparts are found on average for DGPS sources). This is reflected in the high false-positive fraction ($>77\%$). Therefore, the determination of the true counterpart is difficult using XRT positions alone. Through our follow-up campaigns, we found that Chandra observations were pivotal to the identification of the true multiwavelength counterpart (see Section 5.4).

4.1.1. Crossmatch of Non-LSXPS Sources

We performed the same crossmatching analysis outlined in Section 4.1 on the 126 non-LSXPS sources (Figure 7 and Table 3). We find 17 matches in the X-ray catalogs searched, implying that these sources largely comprise a faint, previously undiscovered population of X-ray sources. Of these 17 matches, 12 were in 4XMM-DR9, 7 in 2SXPS, and 7 in CSC 2.0. The sources with matches in these catalogs are marked in Table 3

We further note that a crossmatch of the non-LSXPS sources with SIMBAD results in only 3 classified source matches, and

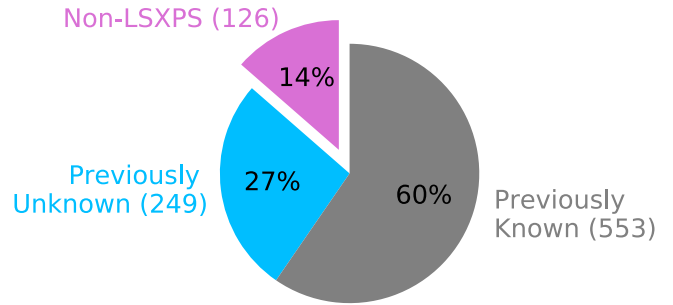


Figure 7. Breakdown of the 928 X-ray sources (802 LSXPS + 126 non-LSXPS) in the full DGPS source catalog.

Table 1

Results of Multiwavelength Crossmatching with External Catalogs Using the Combined 3σ Source Localization

External Catalog	Matches	Spurious Matches
X-ray Catalogs		
2CSC	186	2 (1.0%)
4XMM-DR9	264	3 (1.1%)
2SXPS	463	3 (0.6%)
1SWXRT	63	1 (1.6%)
Unique	249	...
Radio Catalogs		
VLASS	17	1 (5.9%)
Unique	745	...
Optical/Near-infrared Catalogs		
2MASS	689	618 (90.0%)
GAIA	699	635 (90.8%)
USNO-B1	562	431 (76.7%)
Unique	58	...

Note. The expected fraction of spurious matches was determined by shifting our source catalog by $1'-2'$ and rerunning our crossmatching algorithm.

123 sources without a SIMBAD counterpart. Therefore, a significantly larger fraction of those sources not in LSXPS are previously unknown and unclassified, likely due to their faintness and lower number of counterparts in other X-ray catalogs.

While only 17 (13%) of these sources have a known X-ray counterpart, compared to 69% in of those also detected by LSXPS, this further implies (see also Section 3.2.1) that at least some of these non-LSXPS sources are real. Moreover, the fact that seven sources are detected in 2SXPS (Evans et al. 2020) but not in the reanalysis for LSXPS (Evans et al. 2023) emphasizes that the combination of specific observations used to create the mosaic is an important factor in the source detection process.

4.2. Source Classification Breakdown

Our crossmatch with the SIMBAD database (Wenger et al. 2000) resulted in a total of 251 (27%) previously classified sources. However, we found that in some cases the classification was incorrect or incomplete. Thus, while the SIMBAD database provides a useful check as to whether a source is already known (and cross-listings between the same source in

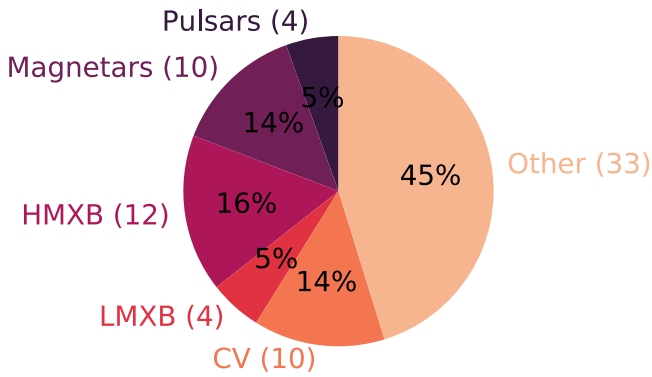


Figure 8. Breakdown of the source type for the 73 classified sources in the full DGPS catalog.

other catalogs), it does not provide a robust measure of the number of confidently classified sources in our catalog.

Therefore, we performed an additional search of other external catalogs containing classified source types, including the McGill Online Magnetar Catalog⁴⁴ (Olausen & Kaspi 2014), HMXBCAT⁴⁵ (Liu et al. 2006), LMXBCAT⁴⁶ (Liu et al. 2007), Australia Telescope National Facility Pulsar Catalogue (Manchester et al. 2005), The Million Quasars (Milliquas) v7.2 Catalogue (Flesch 2021), Symbiotic Stars Catalog⁴⁷ (Belczyński et al. 2000), the New Online Database of Symbiotic Variables⁴⁸ (Merc et al. 2019), X-ray Catalog of Galactic O stars (Nebot Gómez-Morán & Oskinova 2018), Catalog of X-Ray Detected Be Stars⁴⁹ (XDBS; Gobat et al. 2022), a catalog of chromospherically active binary stars (Eker et al. 2008), the Open Cataclysmic Variable Catalog⁵⁰ (Guillochon et al. 2017; Jackim et al. 2020), and intermediate polar (IP) CVs from Koji Mukai’s catalog.⁵¹ This ensures we probe the majority of known sources within these classes.

In total, we find 73 classified sources across the following categories:

- (i) 4 pulsars,
- (ii) 10 magnetars,
- (iii) 12 HMXBs,
- (iv) 4 LMXBs,
- (v) 10 CVs (6 being IPs),
- (vi) 5 Wolf–Rayet (WR) stars,
- (vii) 18 young stellar objects (YSOs),
- (viii) 5 quasars,
- (ix) 3 symbiotic stars,
- (x) and 2 X-ray detected O stars.

The classification breakdown is demonstrated in Figure 8. We do not find any associations with X-ray detected Be stars (Gobat et al. 2022) or chromospherically active binaries (Eker et al. 2008).

⁴⁴ <https://www.physics.mcgill.ca/~pulsar/magnetar/main.html>

⁴⁵ <https://heasarc.gsfc.nasa.gov/W3Browse/all/hmxbcacat.html>

⁴⁶ <https://heasarc.gsfc.nasa.gov/W3Browse/all/lmxbcacat.html>

⁴⁷ <https://heasarc.gsfc.nasa.gov/W3Browse/all/symbiotics.html>

⁴⁸ <http://astronomy.science.upjs.sk/symbiotics/index.html>

⁴⁹ <https://home.gwu.edu/~kargaltsev/XDBS/>

⁵⁰ <https://depts.washington.edu/catvar/index.html>

⁵¹ <https://asd.gsfc.nasa.gov/Koji.Mukai/iphome/catalog/alpha.html> (cross-matched as of 2022 August 31)

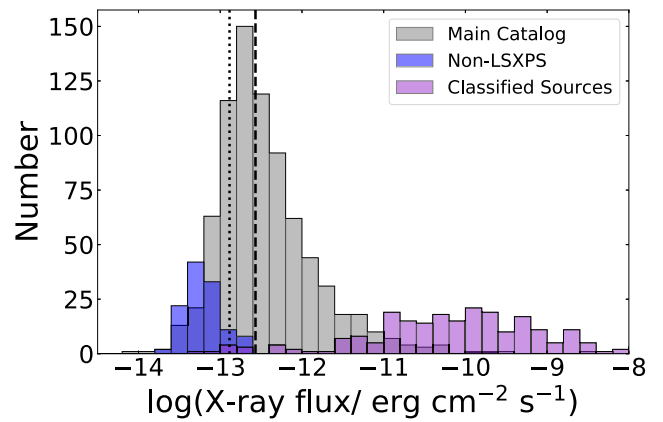


Figure 9. Histogram of average flux values for DGPS sources (gray), the non-LSXPS sources (blue), and known classified sources (purple), including IP CVs, LMXBs, HMXBs, and magnetars. The dotted and dashed lines correspond to the 50% and 90% completeness flux of the DGPS, respectively (see Section 5.1).

Thus, we find only $\sim 9\%$ of DGPS sources are confidently classified. This is likely a lower limit to the true number of classified sources in the survey, given that many of the catalogs searched are over a decade old and may be lacking in completeness. This further emphasizes the need for up-to-date catalogs of source classifications and for machine-learning techniques to determine preliminary source classifications for large data sets (Yang et al. 2021, 2022; Tranin et al. 2022), see Section 5.5.

In Figure 9, we display the X-ray flux distribution of DGPS sources compared to known IP CVs, HMXBs, LMXBs, and magnetars. The large majority of DGPS sources lie below the distribution of classified sources, emphasizing the difficulty in classifying faint sources. This may suggest that the DGPS population of sources could lie at further distances (leading to a lower observed flux), and are therefore possibly more absorbed, due to a larger Galactic column density.

4.3. Variable X-Ray Sources

The DGPS was aimed at uncovering new or variable X-ray sources within the GP. This was done through the rapid analysis of quick-look data (Section 3.1) and the comparison of source flux levels with archival observations. An example of variable sources uncovered in DGPS observations is displayed in Figure 10. The majority of sources displaying obvious variable behavior were already classified (typically HMXBs, LMXBs, or magnetars; Figure 10), but we were also able to classify a number of variable sources (e.g., Gorgone et al. 2019, 2021; O’Connor et al. 2022, 2023a, 2023b) through our follow-up programs, with more classifications in progress.

For the purposes of the DGPS catalog, we make use of the Pearson’s χ^2 variability test (see also Evans et al. 2014, 2020). This test computes the probability that the source count rate is constant across all Swift observations of the source. We consider a source variable if the probability is $P_{\chi, \text{const}} < 0.05$. Approximately half of DGPS sources are expected to display variability (i.e., they are not constant), with a probability higher than 95% (Figure 11).

In addition, following Eyles-Ferris et al. (2022), we compute the ratio of the peak-to-mean X-ray flux, denoted by R_{flux} , as an indicator of flaring sources. We display R_{flux} for each source in Figure 12. We find that only 50 sources in the survey are consistent with $R_{\text{flux}} > 10$ and 138 with $R_{\text{flux}} > 5$. Out of the 50

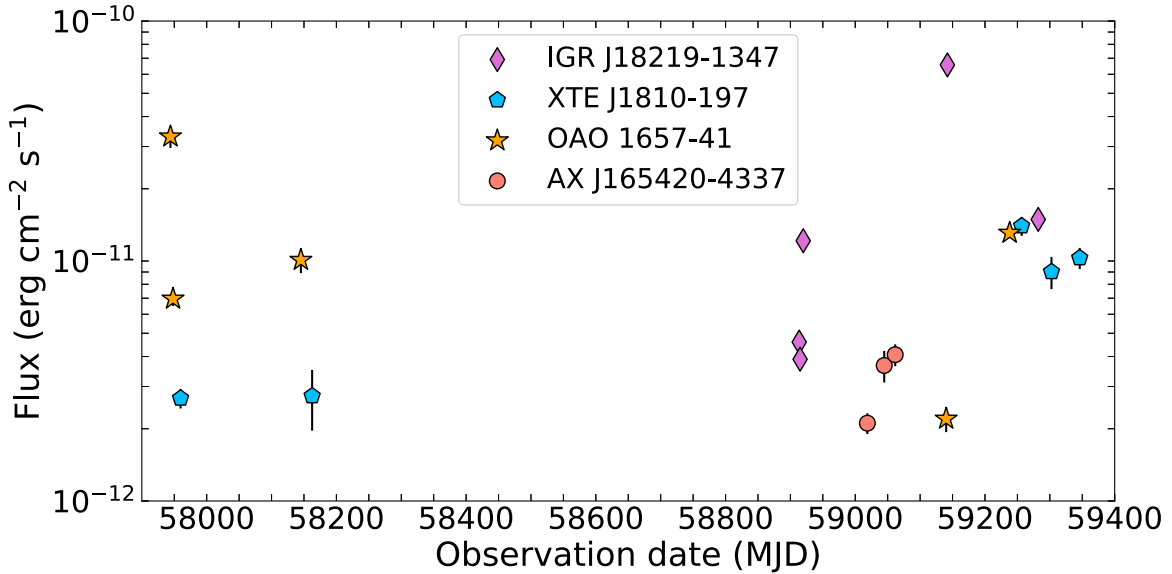


Figure 10. Examples of variable sources identified in DGPS observations: IGR J18219-1347 is a BeXRB (O'Connor et al. 2022), XTE J1810-197 is a magnetar candidate (Markwardt et al. 2003; Israel et al. 2004), OAO 1657-41 is an HMXB (Polidan et al. 1978; Chakrabarty et al. 1993), and AX J165420-4337 (also known as 1RXS J165424.6-433758) is a polar CV (O'Connor et al. 2023a).

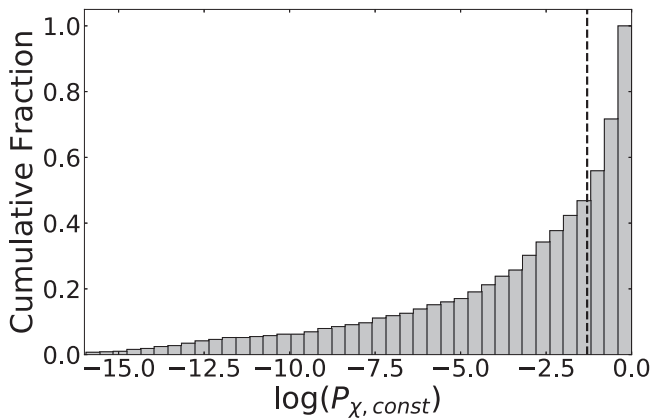


Figure 11. Cumulative distribution of the Pearson's χ^2 variability test for all DGPS sources. The dashed line represents a threshold of $P_{\chi, \text{const}} = 0.05$, below which a source is considered variable. Approximately 50% of sources lie below this threshold.

sources with $R_{\text{flux}} > 10$, only 31 satisfy $F_X/\sigma_{F_X} > 3$ (Figure 12). Thus, only 31 of these sources have accurate enough flux determinations that the increase in flux by an order of magnitude is statistically significant.

If we further sort these to sources with $F_X > 10^{-12}$ erg cm $^{-2}$ s $^{-1}$, our threshold for source follow-up (Section 3.1), we find that only 11 sources satisfy these criterion, all of which are classified and have a known X-ray counterpart: one LMXB, four HMXBs, three magnetars, one pulsar, a pulsar wind nebula (Ng et al. 2008), and the young star cluster Westerlund 1. This is in contrast to a total of 151 sources with $F_X > 10^{-12}$ erg cm $^{-2}$ s $^{-1}$ in the DGPS catalog (115 of which have a known X-ray counterpart).

5. Discussion

5.1. Completeness

We estimated the completeness of the DGPS catalog using the simulations performed by Evans et al. (2014, 2020).

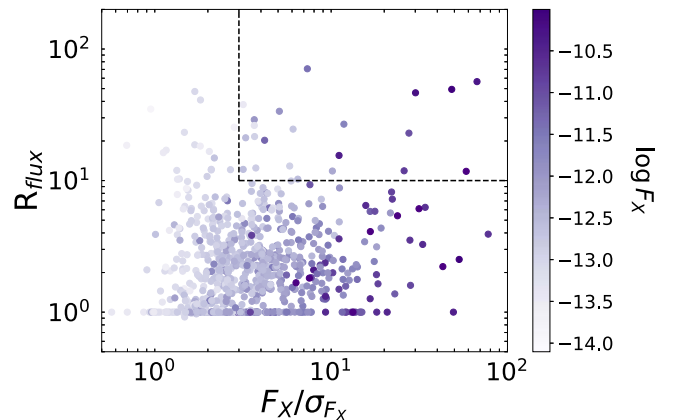


Figure 12. The ratio of the peak-to-mean X-ray flux R_{flux} vs. the ratio of the mean X-ray flux F_X and the X-ray flux error σ_{F_X} . The points are colored by the log of the 0.3–10 keV X-ray flux in erg cm $^{-2}$ s $^{-1}$. The black dashed line indicates a region of parameter space where sources are likely flaring or highly variable.

Evans et al. (2014, 2020) performed detailed simulations of source detection likelihood with Swift/XRT as a function of flux and exposure time. The source detection algorithm utilized in this work is most similar to Evans et al. (2020), which displayed a factor of $3.5 \times$ improvement in sensitivity compared to Evans et al. (2014), due to differences in the detection procedure and a more accurate modeling of the XRT PSF. Therefore, we estimate our completeness using Figure 6 of Evans et al. (2020). We used the simulations corresponding to the inclusion of sources classified as both “good” and “reasonable.”

The median exposure time of DGPS tiles is ~ 4.6 ks. Using the calculations performed by Evans et al. (2020), this corresponds to a 50% completeness flux of 1.3×10^{-13} erg cm $^{-2}$ s $^{-1}$ and a 90% completeness of 2.7×10^{-13} erg cm $^{-2}$ s $^{-1}$. However, as shown in Figure 2, the exposure varies over the GP, due to regions of overlap between tiles. Therefore,

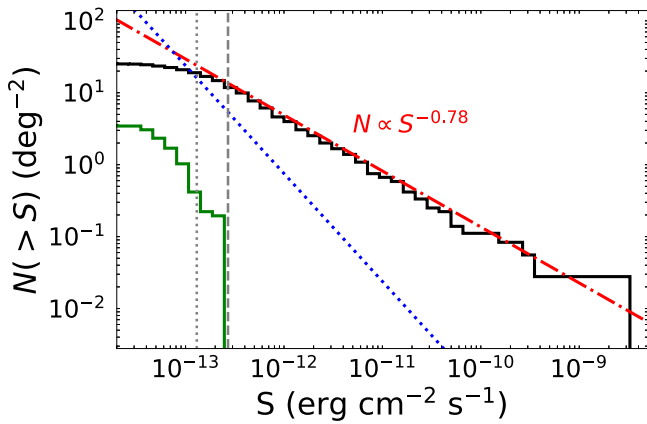


Figure 13. $\log N - \log S$ plot for the full Swift DGPS (0.3–10 keV) catalog. The best-fit line is displayed in red corresponding to $N(>S) \propto S^{-0.78}$. The green solid line displays the $\log N - \log S$ for non-LXSPS sources. The dotted and dashed lines correspond to the 50% and 90% completeness flux of the DGPS, respectively. The blue dotted line is an estimate of the extragalactic source population (Ueda et al. 1999).

these completeness values may underestimate the true fraction of faint sources expected in the overlap regions (see Figure 2).

In order to account for this, we performed a Monte Carlo simulation to sample exposure times from random locations within the survey footprint (Figure 2). We then estimated the 50% and 90% completeness using the same method outlined above. We repeated this procedure for 20,000 locations in order to find a distribution of completeness flux levels across the survey. We find a 50% completeness flux of $(1.3^{+0.3}_{-0.4}) \times 10^{-13}$ erg cm⁻² s⁻¹ and a 90% completeness of $(2.7^{+0.4}_{-0.7}) \times 10^{-13}$ erg cm⁻² s⁻¹. As expected, these values are consistent with our initial estimate.

5.2. Luminosity Function

Using the full DGPS source catalog, we derive the slope and normalization of the $\log N - \log S$ curve at Galactic latitudes $|b| < 0.5$ (Figure 3). We adopt a power-law form of this curve as $N(>S) = KS^\alpha$, where K is a normalization factor. The slope of this curve yields insight into the spatial distribution of X-ray source populations within our Galaxy.

In Figure 13, we display the $\log N - \log S$ derived from the mean fluxes of DGPS sources in the 0.3–10 keV energy range in units of erg cm⁻² s⁻¹. The best-fit power-law distribution has a slope $\alpha = -0.78 \pm 0.03$. We have only fitted the distribution for fluxes above the 50% completeness value (dotted line in Figure 13), where the curve rapidly flattens. We note that including the non-LXSPS sources (Section 3.2.1) has no impact on the value of the slope, as they all lie below the completeness flux value.

Our value is similar to the slope derived with the ASCA GP Survey (Sugizaki et al. 2001) of -0.79 ± 0.07 , and consistent with the -0.64 ± 0.15 slope derived for HMXBs (Grimm et al. 2002). Both values are flatter than the -1 expected for a uniform infinite-plane source distribution. However, past X-ray surveys using different instruments have found values in agreement with $\alpha \approx -1$ (Hertz & Grindlay 1984; Dean et al. 2005). These differences may be due to the survey area covered, with different populations of X-ray sources probed, as well as instrument sensitivity. The DGPS covers regions of the plane dominated by spiral arms (Figure 1) at low Galactic latitudes, and therefore we would expect a shallow slope for the

$\log N - \log S$ relation (Sugizaki et al. 2001; Grimm et al. 2002), whereas past Galactic X-ray surveys also covered larger scale heights, leading to a steeper slope. We note that the $\log N - \log S$ curve for extragalactic X-ray sources is considerably steeper ($\alpha \approx -1.5$; Gioia et al. 1990; Hasinger et al. 1993; Ueda et al. 1999; Luo et al. 2017), and in agreement with the expectations for a 3D Euclidean Universe ($N \propto S^{-3/2}$).

In order to determine whether extragalactic sources visible through the plane were contaminating our sample, we estimated their contribution following the methods of Sugizaki et al. (2001) and by converting the $\log N - \log S$ fit (2–10 keV) from Ueda et al. (1999) to the 0.3–10 keV flux, assuming an extragalactic source spectrum with power-law photon index $\Gamma = 2$ absorbed by $N_H = 5 \times 10^{22}$ cm⁻². These values were chosen under the assumption that the extragalactic source population comprises only active galactic nuclei. The extragalactic population begins to significantly contribute at fluxes less than 10^{-12} erg cm⁻² s⁻¹, and it has a negligible impact on the population of brighter sources.

5.3. Catalog Characteristics

Figure 14 shows the 0.3–10 keV X-ray flux versus HR₁ and HR₂ for DGPS sources. For comparison, we display the known population of IP CVs, LMXBs (Liu et al. 2007), HMXBs (Liu et al. 2006), and magnetars (Olausen & Kaspi 2014) from the 2SXPS catalog (see Appendix C for details). We see that the majority of our sources lie both below the completeness values (vertical lines) and below the flux of classified sources (Figure 9), underscoring a very large population of faint, unclassified sources. However, it is difficult to classify these sources based on hardness ratios alone, as demonstrated by Figure 15 (for details, see Appendix C). There is significant overlap in the population of classified sources, emphasizing the need for machine learning to disentangle source properties in higher-dimensional space (Yang et al. 2022; Tranin et al. 2022).

The DGPS sources are distributed relatively uniformly across Galactic longitude (Figures 16 and 17) within the survey footprint (Section 2). For example, the number of sources between $10 < l < 30$ deg and $330 < l < 350$ deg is 413 and 389, respectively. However, pockets of longitude with less sources exist. We find that this is due, at least in part, to sources of intense stray light (Figure 3) at $l \approx 338$ –342 deg and $l \approx 12$ –14 deg (see the black star in Figure 17; bottom panel). This is caused by the fact that we excluded sources with an LXSPS field flag indicating that they reside in regions of stray light—and therefore may be the result of unreliable detections (Section 3.2). In Galactic latitude, we see a marked decrease in sources as we move away from the GP, as expected. In Appendix B, we display additional characteristics of sources across the GP (e.g., hardness ratios and variability).

5.4. New or Newly Classified Sources

We followed up unclassified, variable sources using our approved ToOs on Chandra, NuSTAR, NICER, and XMM-Newton, including XMM-Newton AO17 (Proposal ID: 082186; PI: Kouveliotou), Chandra Cycles 19, 20, and 23 (Proposal IDs: 19500723, 20500298, and 23500070; PI: Kouveliotou), and NICER Cycle 3 and 4 (Proposal IDs: 4050 and 5097; PI: Kouveliotou). The DGPS was a NuSTAR Legacy Survey until 2019, although since this time we have

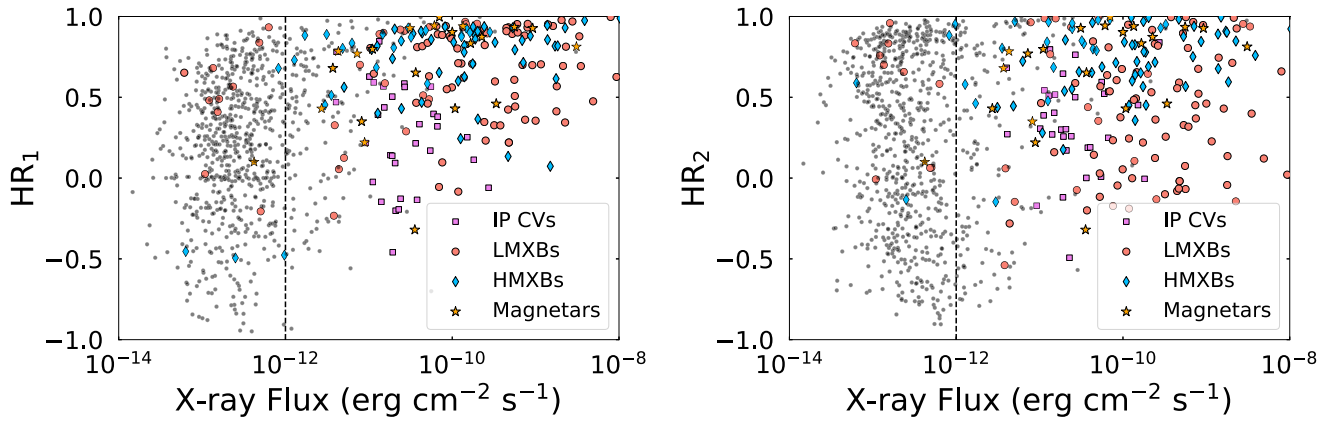


Figure 14. Distribution of DGPS sources (gray circles) in terms of hardness ratio and X-ray flux. For reference, we display LMXBs, IP CVs, HMXBs, and magnetars from the 2SXPS catalog.

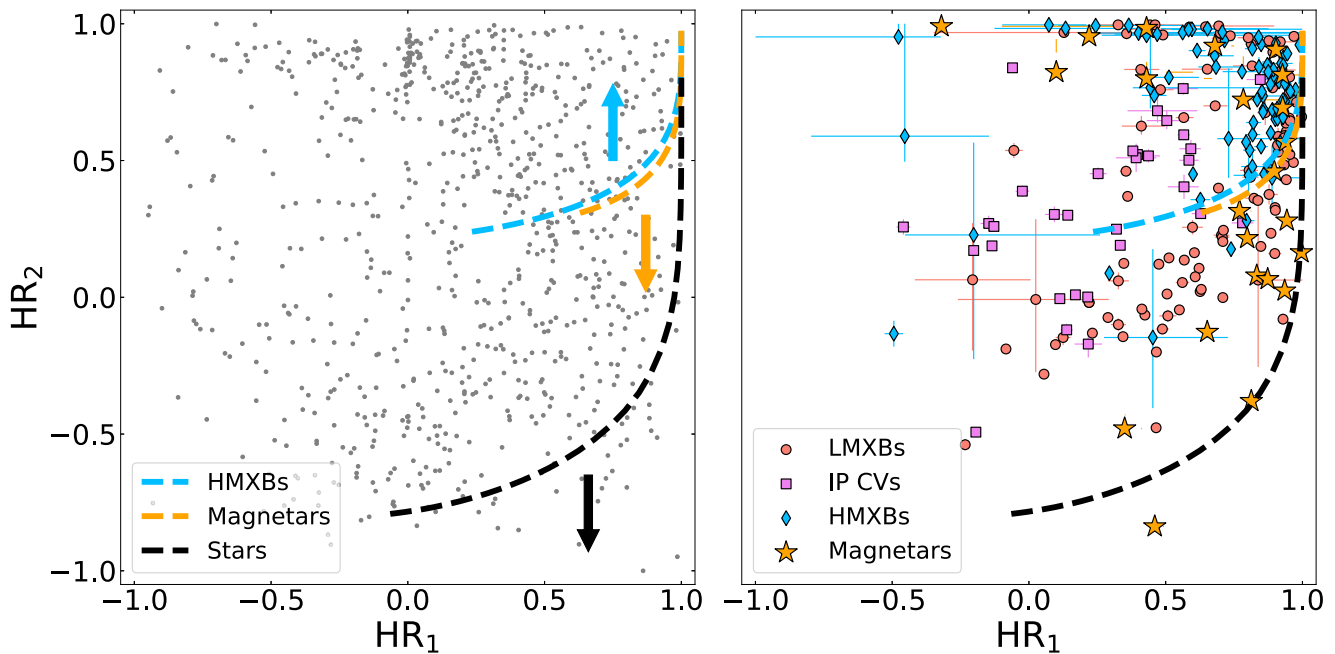


Figure 15. Left: locations of DGPS sources (gray circles) in the $HR_1 - HR_2$ plane. The dashed lines represent typical spectra for HMXBs, magnetars, and stars as outlined in Appendix C. The arrows mark the general location of these sources with respect to the lines. Right: the mean hardness ratios of LMXBs, IP CVs, HMXBs, and magnetars from 2SXPS are shown for comparison.

utilized Director’s Discretionary Time observations. In total, we carried out three XMM-Newton ToOs, nine NuSTAR ToOs, nine Chandra ToOs, six NICER ToOs, and 20 Swift ToOs to follow DGPS sources. In addition, we made use of multiwavelength observations from the Lowell Discovery Telescope, the South African Astronomical Observatory 1.0 m telescope, and the Southern African Large Telescope. The results of these campaigns were reported in Gorgone et al. (2019, 2021), O’Connor et al. (2022, 2023a, 2023b).

5.5. Machine-learning Classification of DGPS Sources

As shown in Section 4.2, the DGPS has detected a large number of unclassified X-ray sources. The classification of hundreds of X-ray sources based on manual compilation and analyses of multiwavelength data sets is difficult and time consuming. Instead, it is more efficient to turn to supervised machine-learning methods to perform the classification of a large number of sources based on the properties of a training

data set comprising sources with already known classes. Yang et al. (2022) performed such analysis for a subset of the Chandra Source Catalog version 2.0 (CSCv2) using a publicly available⁵² Python framework and a training data set of ~ 3000 sources with verified classifications.⁵³ They first applied a selection criterion to CSCv2 to remove Chandra sources with low signal-to-noise ratios or poor localization errors, as well as those that were either extended or confused (see Yang et al. 2022 for details). The sources satisfying their criteria are referred to as “good” CSCv2 sources (GCS). In total, they are able to provide classifications to 66,359 CSCv2 sources, approximately 21% of the CSCv2 catalog.

While Yang et al. (2022) have not yet extended their analysis to other X-ray missions (see, however, Tranin et al. 2022), their results can provide useful insight into the classification of a

⁵² https://github.com/huiyang-astro/MUWCLASS_CSCv2

⁵³ <https://home.gwu.edu/~kargaltsev/XCLASS/>

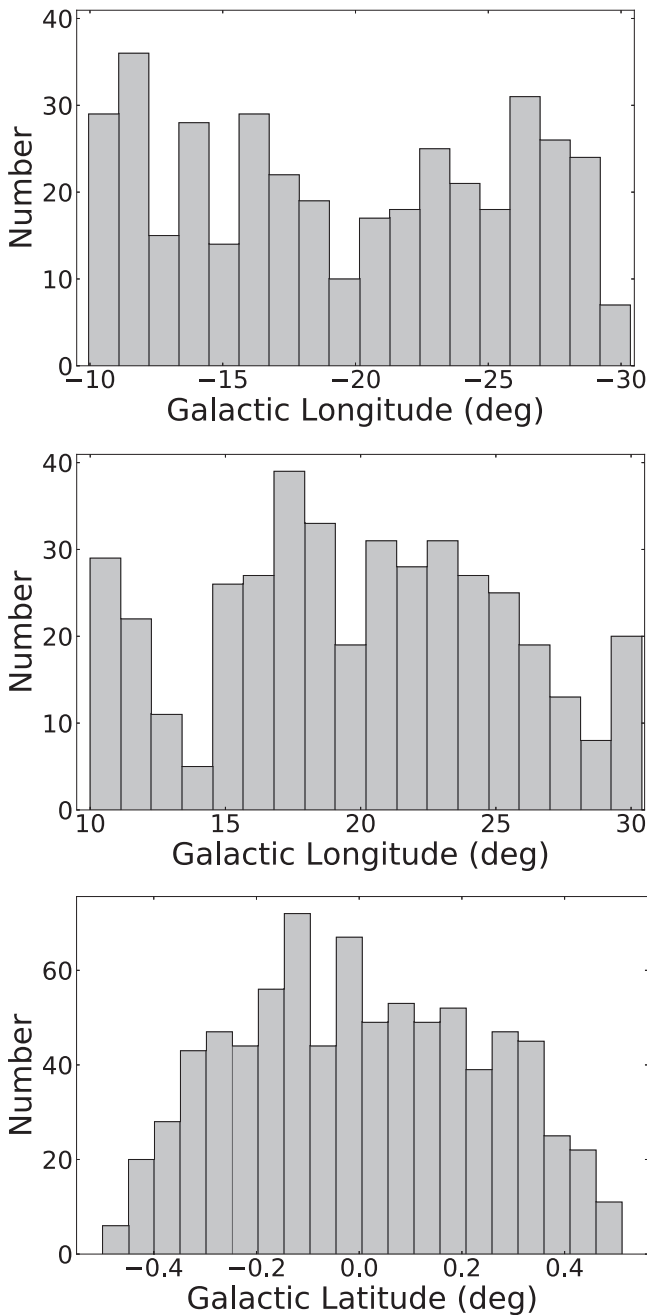


Figure 16. Histograms of the number of sources detected per Galactic longitude on both sides of the plane and in Galactic latitude (combining both sides of the plane). We note that the dip in sources at $l \approx 14$ deg and 340 deg is due to stray light contaminating those fields.

subset of DGPS sources. We note that one of the main obstacles for extending these analyses to Swift is the significantly larger localization uncertainties of X-ray sources precluding accurate multiwavelength crossmatching. Therefore, below we only review the classifications of DGPS sources that have counterparts in CSCv2, which provide much more accurate positions.

After performing a crossmatch between DGPS sources and the CSCv2 catalog, we find 186 matches (Table 1). We then matched these sources to the results of Yang et al. (2022), finding 45 classified GCSs in addition to 19 sources in their training data set. These sources have a classification confidence threshold (CT) indicating the confidence level, with $CT \geq 2$

adopted for confidently classified GCSs (CCGCSs). Out of the 45 GCS sources, only eight are CCGCSs. In Figure 18, we display the classification stacked histogram of all 45 sources. The largest number of CCGCSs are four YSOs, followed by three NSs, and one CV.

Although three NS candidates (2CXO J171428.6–383601, 2CXO J182524.7–114524, and 2CXO J181210.3–184208), which each lack any optical or infrared counterpart, have been confidently classified, this may be due to a bias in the training data set against faint sources without multiwavelength counterparts. A large fraction of faint sources do not have multiwavelength counterparts simply because of the insufficient sensitivity of optical and infrared surveys combined with the significant extinction in the GP. The classification algorithm of Yang et al. (2022) may instead interpret the lack of multiwavelength counterparts as a sign of the NS class (which includes both magnetars and isolated NSs). Indeed, upon further investigation, two out of three of these NS candidates (2CXO J182524.7–114524 and 2CXO J181210.3–184208) have infrared counterparts in UKIDSS, which is significantly more sensitive than the 2MASS catalog used in Yang et al. (2022). The third source (2CXO J171428.6–383601) may have an infrared counterpart in VVV, but the source lies outside of the 95% localization region ($0''.9$) from CSCv2 at an offset of $1''.2$. Based on the VVV sky density in this region of the GP, we compute a probability of chance coincidence of between 25% and 37%, depending on whether or not we account for the brightness of the counterpart.

5.6. Constraints on the Population of Magnetars

The main targets of the Swift DGPS were magnetars and HMXBs. However, although several of the already known sources from both populations were observed (Figure 8), we did not concretely identify any new transient events associated with magnetars, and we classified only a single new HMXB (O'Connor et al. 2022).

Magnetars are generally identified during their bright X-ray outbursts. As such, the quiescent magnetar population is poorly constrained. Using the Magnetar Outburst Online Catalog⁵⁴ (Coti Zelati et al. 2018), we compiled the distance and quiescent X-ray (0.3–10 keV) luminosity for 15 magnetars. Their observed quiescent luminosities lie between 10^{30-35} erg s^{-1} (Coti Zelati et al. 2018). Using the best available distance for each event, we find quiescent X-ray fluxes in the range $10^{-15}-10^{-12}$ erg cm^{-2} s^{-1} . Therefore, only 7 out of 15 magnetars would be detectable based on the DGPS 50% completeness flux.

For example, we note here that the DGPS observed the field of the magnetar Swift J1818.0–1607 (Blumer & Safi-Harb 2020; Champion et al. 2020; Hu et al. 2020) approximately 2.7 yr before its discovery. Unfortunately, the source was not active and we were only able to obtain an upper limit (3σ) of $\lesssim 2 \times 10^{-13}$ erg cm^{-2} s^{-1} . This demonstrates that quiescent magnetars exist in the region covered by the DGPS, but their identification is difficult, possibly due to faintness. A significant benefit of this survey is to constrain the quiescent luminosity of future magnetars, or other transients, discovered in these regions.

In fact, Beniamini et al. (2019) found that, based on the observed persistent luminosity and $\log N - \log S$ distribution,

⁵⁴ <http://magnetars.ice.csic.es/#/welcome>

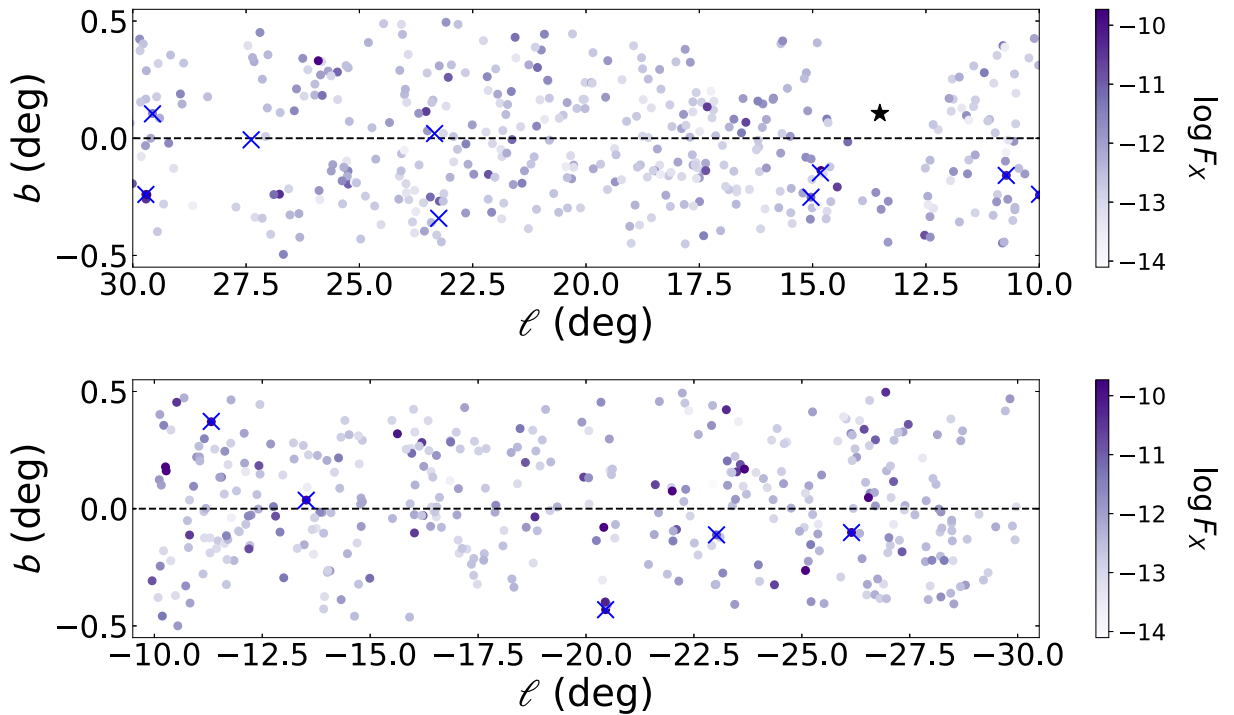


Figure 17. The location of DGPS sources in Galactic coordinates. The sources are colored based on the logarithm of their X-ray flux. The blue crosses show the locations of known magnetars. The black star (bottom panel) marks a dominant source of stray light, leading to an obvious lack of sources at that region of the survey.

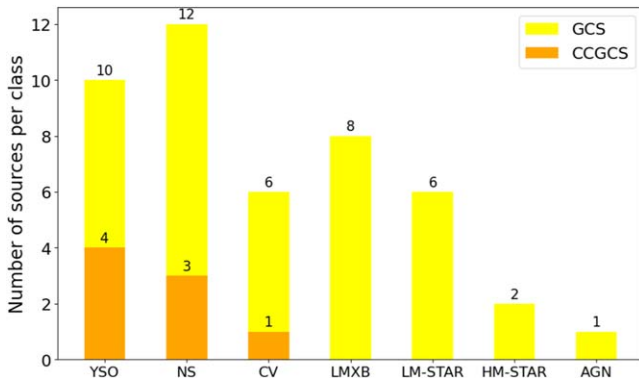


Figure 18. Histogram of source classification breakdown for 45 GCSs and eight CCGCSs based on results from Yang et al. (2022).

the number of hidden magnetars could outweigh the known population by a factor of up to ~ 10 . They found that the missing magnetars should have unabsorbed fluxes $< 10^{-13}$ erg cm^{-2} s^{-1} , which is below the DGPS completeness values.

In the general spin-down model for magnetars, the magnetic field evolution is parameterized by $\dot{B} \propto B^{1+\alpha}$ (Colpi et al. 2000). Beniamini et al. (2019) used the observed $\log N - \log S$ for magnetars to show that both $\alpha = 0$ and -1 can explain the observed population of absorbed and unabsorbed magnetar fluxes. We perform a similar calculation using the constraints of our survey. Based on the DGPS $\log N - \log S$ (Figure 13), we have detected 144 sources at $> 1.0 \times 10^{-12}$ erg cm^{-2} s^{-1} , of which 10 are known magnetars (Figure 8), and 400 sources at $> 2.7 \times 10^{-13}$ erg cm^{-2} s^{-1} (including the 144 mentioned above). Under the assumption that none of these new sources are magnetars, we constrain $\alpha < -0.65$ at the 90% confidence level. We note that the assumption that none of the ~ 1000 sources in our survey are magnetars is likely too restrictive, as

there could be unidentified quiescent magnetars hiding in this population. If instead we assume there are 10 (20) unidentified magnetars with a flux between 2.7×10^{-13} and 1.0×10^{-12} erg cm^{-2} s^{-1} , the constraint is $\alpha < 0.86$ (2.15). These results are consistent with Beniamini et al. (2019).

The upper limit to α is therefore strongly dependent on the unknown population of unidentified quiescent magnetars hiding in our sample. Nevertheless, the identification of their quiescent population is extremely difficult. This issue was explored in detail by Munro et al. (2008) using constraints from XMM-Newton and Chandra. They searched for periodic variability in deep X-ray observations of the GP region ($|b| < 5$ deg), but did not identify any new periods between 5 and 20 s. Based on their analysis, Munro et al. (2008) found that < 540 magnetars (90% confidence level) should exist in the Milky Way. Due to the lower exposure times and photon counts of our survey compared to the deep XMM-Newton and Chandra data used by Munro et al. (2008), a timing analysis of our sources is not as fruitful.

6. Conclusions

We have presented the results of the DGPS Phase I observations, covering Galactic longitude $10 < |l| < 30$ deg and latitude $|b| < 0.5$ deg. These observations led to the identification of 928 unique X-ray sources (Tables 2 and 3) of which 358 (40%) were previously unknown to other X-ray surveys. Our results indicate a significant population of very faint X-ray sources below $F_X < 10^{-13}$ erg cm^{-2} s^{-1} , emphasizing the necessity for sensitive, next-generation, wide-field X-ray telescopes, e.g., Athena (Nandra et al. 2013), AXIS (Mushotzky et al. 2019), Lynx (Gaskin et al. 2019), and STAR-X (Zhang et al. 2022), to characterize the missing faint X-ray population in our Galaxy.

Acknowledgments

The authors thank the anonymous referee for constructive feedback that improved the manuscript. B.O. and C.K. acknowledge support from multiple grants to follow-up DGPS sources: NASA grants 80NSSC17K0335, 80NSSC20K0389, 80NSSC19K0916, 80NSSC22K1398, and 80NSSC22K0583, Chandra awards GO9-20057X and GO2-23038X, and award number 46939-1-CCNS 22317F. P.B.'s research was supported by a grant (No. 2020747) from the United States–Israel Binational Science Foundation (BSF), Jerusalem, Israel. J.H. and Z.W. acknowledge support from NASA under award No. 80GSFC21M0002.

This work made use of data supplied by the UK Swift Science Data Centre at the University of Leicester. This research has made use of the XRT Data Analysis Software (XRTDAS) developed under the responsibility of the ASI Science Data Center (ASDC), Italy. This research has made use of the VizieR catalog access tool, CDS, Strasbourg, France (<https://vizier.cds.unistra.fr>). The original description of the VizieR service was published in Ochsenbein et al. (2000). This research has made use of the SIMBAD database, operated at

CDS, Strasbourg, France. This research has made use of data obtained from the Chandra Source Catalog, provided by the Chandra X-ray Center (CXC) as part of the Chandra Data Archive. This research has made use of data obtained from the 4XMM XMM-Newton serendipitous source catalog compiled by the 10 institutes of the XMM-Newton Survey Science Centre selected by ESA. This research has made use of data and/or software provided by the High Energy Astrophysics Science Archive Research Center (HEASARC), which is a service of the Astrophysics Science Division at NASA/GSFC.

Facility: Swift (XRT).

Software: HEASo_{ft}, XRTDAS, swifttools (Evans et al. 2023), PIMMS, Astropy (Astropy Collaboration et al. 2013).

Appendix A Additional GP Mosaics

Here, we present additional mosaics of the DGPS observations in the SB, MB, and HB (Figures 19 and 20). These mosaics complement the FB image of the plane displayed in Figure 3.

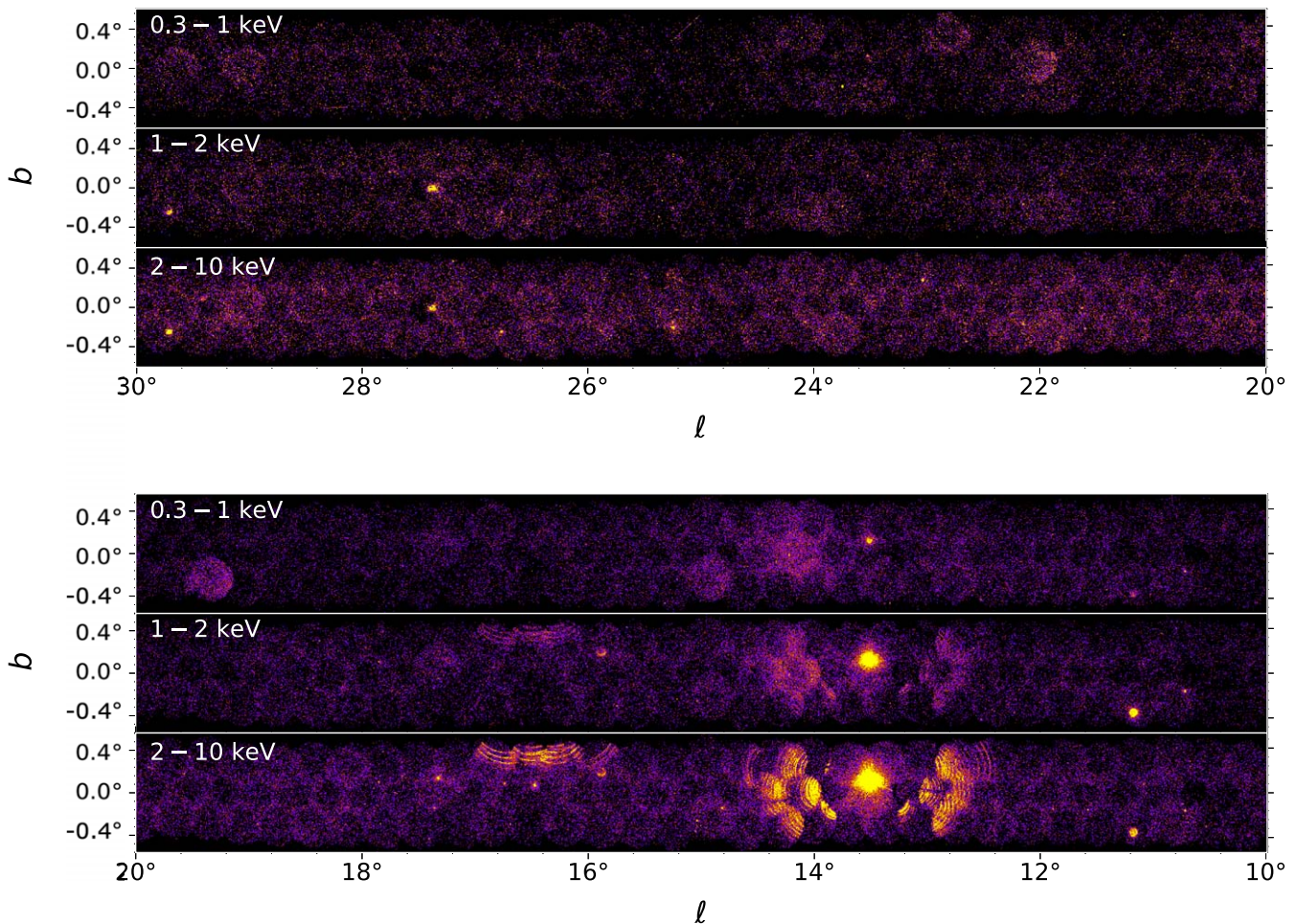


Figure 19. Mosaic of the GP at positive Galactic longitudes in the SB (0.3–1 keV), MB (1–2 keV), and HB (2–10 keV).

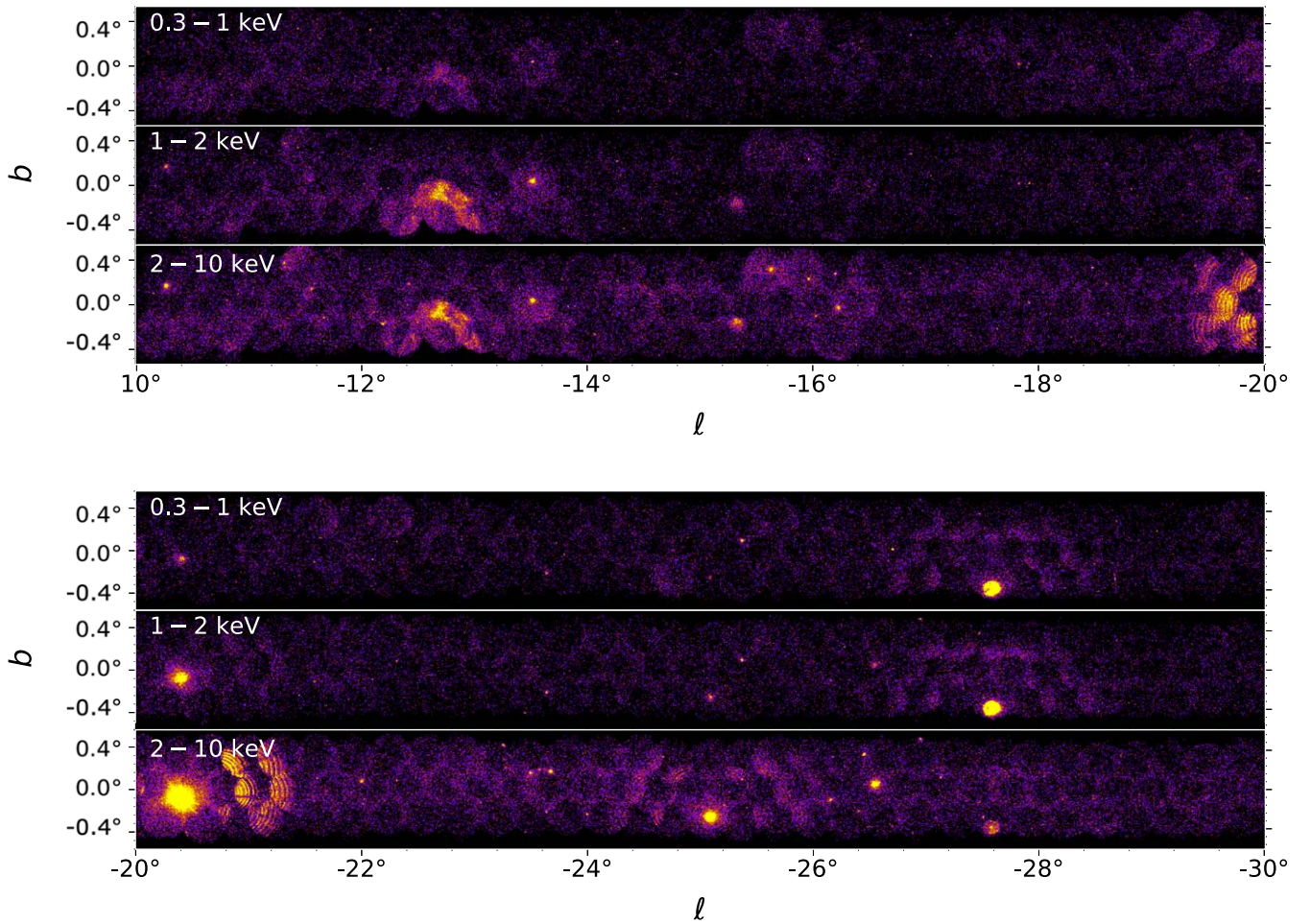


Figure 20. Mosaic of the GP at negative Galactic longitudes in the SB (0.3–1 keV), MB (1–2 keV), and HB (2–10 keV). The background variation across the plane is due to higher exposure in regions with overlapping tiles and is not due to an intrinsic structure in the emission.

Appendix B

Comparison of Source Properties in Galactic Coordinates

Here, we present additional figures demonstrating how source properties vary with location in the Galactic plane. Figure 21 shows the hardness ratio for each source versus their location in Galactic coordinates. There appears to be a clustering of sources in HR_2 , but less so in HR_1 . We note that the hardness ratios are uncorrected for Galactic hydrogen column density, and that a line-of-sight absorption effect may be at play here.

In Figure 22 (left), we show a histogram of Galactic latitude for variable and constant sources. There is no discernible difference, and a Kolmogorov–Smirnov test supports the null hypothesis (p -value = 0.7) that they are drawn from the same distribution.

We also show the source distribution in the hardness ratio plane separated between $|b| < 0.1$ deg and $|b| > 0.1$ deg (Figure 22; right). There is no obvious clustering of sources based on this separation criterion.

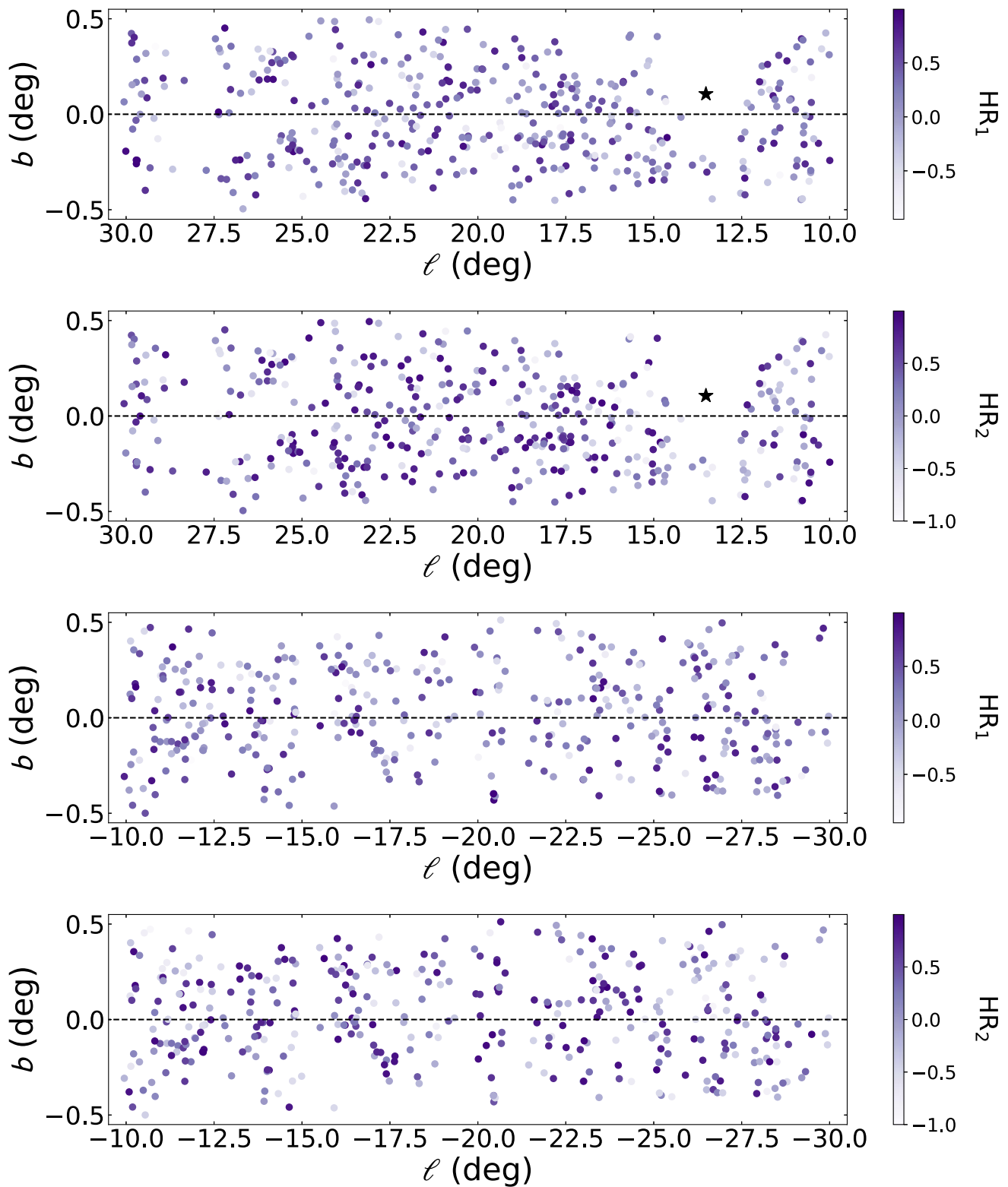


Figure 21. The location of DGPS sources in Galactic coordinates. The sources are colored based on their hardness ratio (either HR_1 or HR_2). The black star (bottom panels) marks a dominant source of stray light, leading to an obvious lack of sources in that region of the survey.

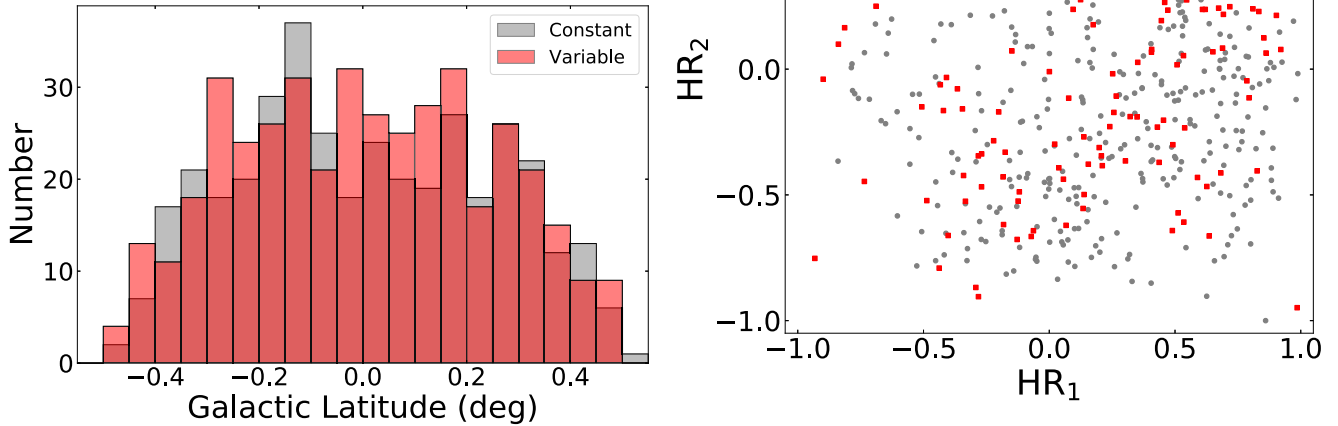


Figure 22. Left: histogram of source location in Galactic latitude for constant (gray) and variable (red) sources (see Section 4.3). Right: distribution of sources in the hardness ratio plane. Red squares are sources on the GP with $|b| < 0.1$ deg, and gray circles are off-plane sources with $|b| > 0.1$ deg.

Appendix C Derivation of Hardness Ratios for X-Ray Source Populations

The majority of sources detected with the DGPS are faint, with a low number of source counts (i.e., < 30 counts), and therefore an analysis of their X-ray spectra does not provide strong constraints on the intrinsic source properties. Therefore, we utilized the X-ray hardness ratios, comparing the count rate between different energy bands, as a way to characterize source spectra despite the small number of counts. The hardness ratios HR_1 and HR_2 are defined as in Evans et al. (2014, 2020):

$$HR_1 = \frac{MB - SB}{MB + SB} \text{ and } HR_2 = \frac{HB - MB}{HB + MB}, \quad (C1)$$

where $SB = 0.3\text{--}1$ keV, $MB = 1\text{--}2$ keV, and $HB = 2\text{--}10$ keV count rate. The use of two hardness ratios is ideal for characterizing soft sources and distinguishing between different source classifications.

In order to characterize the expected location of different source classes in the $HR_1 - HR_2$ plane, we assumed spectral properties belonging to each class and varied the hydrogen column density (see also Rigoselli et al. 2022). We did this for HMXBs assuming a power-law spectrum with photon index $\Gamma = 1$, for stars assuming an APEC spectrum with temperature $kT = 1.085$ keV and 0.6 solar abundance, and for magnetars assuming a blackbody with $kT = 1$ keV. We varied the hydrogen column density uniformly between $\log(N_H/\text{cm}^{-2}) = 18\text{--}23$. We performed this calculation using PIMMS to compute the Swift/XRT count rate in the SB, MB, and HB at each step in the grid. We then determined both hardness ratios based on these values. We show the tracks of each source type in Figure 15. The majority of stars have thermal plasma temperatures less than $kT < 1$ keV, such that they lie below the line in $HR_1 - HR_2$ space. Similarly, many HMXBs display harder spectra than $\Gamma = 1$, and for that reason they lie above the

line in $HR_1 - HR_2$ space. In the case of magnetars, their quiescent spectra are generally described by a softer blackbody with $kT \approx 0.4$ keV (Coti Zelati et al. 2017), suggesting that quiescent magnetars will lie below the line drawn.

We further checked the observed location of different source classes in the $HR_1 - HR_2$ plane by obtaining the observed mean flux and mean hardness ratios from the 2SXPS catalog. In Figure 15 (right), we show the observed locations for magnetars from the McGill Online Magnetar Catalog (Olausen & Kaspi 2014), HMXBs from Liu et al. (2006), LMXBs from Liu et al. (2007), and IP CVs from Koji Mukai's online catalog. As expected, many HMXBs lie above our computed line for $\Gamma = 1$. Of further note is the broad diversity observed for magnetars, possibly due to the observed outbursts by Swift and the spectral cooling of the sources during outburst (Coti Zelati et al. 2018).

Appendix D Tables of Catalog Contents

Here, we provide a description of the contents available for the DGPS catalog:

1. Sources with additional information pulled from LSXPS (Table 2).
2. Sources not in LSXPS (Table 3).

The main difference between the catalogs is the availability of variability and hardness ratio information. Both catalogs comprise the full result of the DGPS Phase I.

In these tables, the energy bands are coordinated such that they agree with the Evans et al. (2023) definitions: band0 is the full band (FB; 0.3–1 keV), band1 is the soft band (SB; 0.3–10 keV), band2 is the medium band (MB; 1–2 keV), and band3 is the HB (HB; 2–10 keV).

Table 2
Contents for DGPS Sources for Which We Were Able to Pull Additional Information from LSXPS

Column	Units	Description
IAU Name		IAU name in format “DGPS JHHMMSS.S ± DDMMSS”
LSXPS_ID		Numerical unique source identifier within LSXPS
RA	deg	R.A. (J2000)
DEC	deg	Decl. (J2000)
Err90	arcsec	90% source position uncertainty
l	deg	Galactic longitude
b	deg	Galactic latitude
Rate_band0	counts s ⁻¹	FB (0.3–10 keV) count rate
Rate_band0_pos	counts s ⁻¹	Positive count rate error
Rate_band0_neg	counts s ⁻¹	Negative count rate error
Rate_band1	counts s ⁻¹	SB (0.3–1 keV) count rate
Rate_band1_pos	counts s ⁻¹	Positive count rate error
Rate_band1_neg	counts s ⁻¹	Negative count rate error
Rate_band2	counts s ⁻¹	MB (1–2 keV) count rate
Rate_band2_pos	counts s ⁻¹	Positive count rate error
Rate_band2_neg	counts s ⁻¹	Negative count rate error
Rate_band3	counts s ⁻¹	HB (2–10 keV) count rate
Rate_band3_pos	counts s ⁻¹	Positive count rate error
Rate_band3_neg	counts s ⁻¹	Negative count rate error
FixedPowUnabsFlux	erg cm ⁻² s ⁻¹	FB X-ray flux (0.3–10 keV) assuming a photon index $\Gamma = 1.7$
FixedPowUnabsFlux_pos	erg cm ⁻² s ⁻¹	Positive flux error
FixedPowUnabsFlux_neg	erg cm ⁻² s ⁻¹	Negative flux error
R_Flux		Ratio of peak-to-mean flux
HR1		Hardness ratio between the MB and SB
HR1_pos		Positive error on hardness ratio
HR1_neg		Negative error of hardness ratio
HR2		Hardness ratio between the HB and MB
HR2_pos		Positive error on hardness ratio
HR2_neg		Negative error of hardness ratio
GalacticNH	cm ⁻²	Hydrogen column density in the source direction (Willingale et al. 2013)
Exposure	s	Cumulative DGPS exposure at the source position
X-ray Match		“Y” if known X-ray source, otherwise “N”
Variable		“Y” if known source is variable, otherwise “N”

Note. The table is accessible in electronic form through Vizier (Ochsenbein et al. 2000).

(This table is available in its entirety in machine-readable form.)

Table 3
Contents for the Non-LSXPS Sources

Column	Units	Description
IAU Name		IAU name in format “DGPS JHHMMSS.S ± DDMSS”
RA	deg	R.A. (J2000)
DEC	deg	Decl. (J2000)
Err90	arcsec	90% source position uncertainty
X-ray Match		“Y” if known X-ray source, otherwise “N”
band0_KNB91_Detected		Source retrospectively detected in FB using LSXPS Upper Limit Server (0 = not detected; 1 = detected)
band3_KNB91_Detected		Source retrospectively detected in HB using LSXPS Upper Limit Server
band2_KNB91_Detected		Source retrospectively detected in MB using LSXPS Upper Limit Server
band1_KNB91_Detected		Source retrospectively detected in SB using LSXPS Upper Limit Server
band0_IsDetected		Source blindly detected in FB through iterative source detection on mosaics (0 = not detected; 1 = detected)
band3_IsDetected		Source blindly detected in HB through iterative source detection on mosaics
band2_IsDetected		Source blindly detected in MB through iterative source detection on mosaics
band1_IsDetected		Source blindly detected in SB through iterative source detection on mosaics
Rate_band0	counts s ⁻¹	FB (0.3–10 keV) count rate
Rate_band0_pos	counts s ⁻¹	Positive count rate error
Rate_band0_neg	counts s ⁻¹	Negative count rate error
Rate_band3	counts s ⁻¹	HB (2–10 keV) count rate
Rate_band3_pos	counts s ⁻¹	Positive count rate error
Rate_band3_neg	counts s ⁻¹	Negative count rate error
Rate_band2	counts s ⁻¹	MB (1–2 keV) count rate
Rate_band2_pos	counts s ⁻¹	Positive count rate error
Rate_band2_neg	counts s ⁻¹	Negative count rate error
Rate_band1	counts s ⁻¹	SB (0.3–1 keV) count rate
Rate_band1_pos	counts s ⁻¹	Positive count rate error
Rate_band1_neg	counts s ⁻¹	Negative count rate error
FixedPowUnabsFlux	erg cm ⁻² s ⁻¹	FB X-ray flux (0.3–10 keV) assuming a photon index $\Gamma = 1.7$
FixedPowUnabsFlux_pos	erg cm ⁻² s ⁻¹	Positive flux error
FixedPowUnabsFlux_neg	erg cm ⁻² s ⁻¹	Negative flux error

Note. These are sources with no LSXPS counterpart. The table is accessible in electronic form through VizieR (Ochsenbein et al. 2000).

(This table is available in its entirety in machine-readable form.)

ORCID iDs

B. O’Connor  <https://orcid.org/0000-0002-9700-0036>
C. Kouveliotou  <https://orcid.org/0000-0003-1443-593X>
P. A. Evans  <https://orcid.org/0000-0002-8465-3353>
N. Gorgone  <https://orcid.org/0000-0002-1653-6411>
A. J. van Kooten  <https://orcid.org/0000-0002-3905-4853>
S. Gagnon  <https://orcid.org/0000-0003-0902-1935>
H. Yang  <https://orcid.org/0000-0002-8832-6077>
M. G. Baring  <https://orcid.org/0000-0003-4433-1365>
E. Bellm  <https://orcid.org/0000-0001-8018-5348>
P. Beniamini  <https://orcid.org/0000-0001-7833-1043>
J. Brink  <https://orcid.org/0000-0003-0030-7566>
D. A. H. Buckley  <https://orcid.org/0000-0002-7004-9956>
S. B. Cenko  <https://orcid.org/0000-0003-1673-970X>
O. D. Egbo  <https://orcid.org/0009-0001-0232-3968>
E. Göğüş  <https://orcid.org/0000-0002-5274-6790>
J. Granot  <https://orcid.org/0000-0001-8530-8941>
C. Hailey  <https://orcid.org/0000-0002-3681-145X>
J. Hare  <https://orcid.org/0000-0002-8548-482X>
F. Harrison  <https://orcid.org/0000-0002-4226-8959>
D. Hartmann  <https://orcid.org/0000-0002-8028-0991>
A. J. van der Horst  <https://orcid.org/0000-0001-9149-6707>
D. Huppenkothen  <https://orcid.org/0000-0002-1169-7486>
O. Kargaltsev  <https://orcid.org/0000-0002-6447-4251>
J. A. Kennea  <https://orcid.org/0000-0002-6745-4790>
K. Mukai  <https://orcid.org/0000-0002-8286-8094>
P. O. Slane  <https://orcid.org/0000-0002-6986-6756>

D. Stern  <https://orcid.org/0000-0003-2686-9241>
E. Troja  <https://orcid.org/0000-0002-1869-7817>
Z. Wadiasingh  <https://orcid.org/0000-0002-9249-0515>
R. A. M. J. Wijers  <https://orcid.org/0000-0002-3101-1808>
P. Woudt  <https://orcid.org/0000-0002-6896-1655>
G. Younes  <https://orcid.org/0000-0002-7991-028X>

References

- Astropy Collaboration, Robitaille, T. P., Tollerud, E. J., et al. 2013, *A&A*, **558**, A33
Bahramian, A., Heinke, C. O., Kennea, J. A., et al. 2021, *MNRAS*, **501**, 2790
Barrett, P., Singh, K. P., & Mitchell, S. 1999, in ASP Conf. Ser. 157, Annapolis Workshop on Magnetic Cataclysmic Variables, ed. C. Hellier & K. Mukai (San Francisco, CA: ASP), 180
Belczyński, K., Mikołajewska, J., Munari, U., Ivison, R. J., & Friedjung, M. 2000, *A&AS*, **146**, 407
Beniamini, P., Hotokezaka, K., van der Horst, A., & Kouveliotou, C. 2019, *MNRAS*, **487**, 1426
Blumer, H., & Safi-Harb, S. 2020, *ApJL*, **904**, L19
Burrows, D. N., Hill, J. E., Nousek, J. A., et al. 2005, *SSRv*, **120**, 165
Chakrabarty, D., Grunsfeld, J. M., Prince, T. A., et al. 1993, *ApJL*, **403**, L33
Champion, D., Cognard, I., Cruces, M., et al. 2020, *MNRAS*, **498**, 6044
Colpi, M., Geppert, U., & Page, D. 2000, *ApJL*, **529**, L29
Coti Zelati, F., Rea, N., Pons, J. A., Campana, S., & Esposito, P. 2018, *MNRAS*, **474**, 961
Coti Zelati, F., Rea, N., Turolla, R., et al. 2017, *MNRAS*, **471**, 1819
Dean, A. J., Bazzano, A., Hill, A. B., et al. 2005, *A&A*, **443**, 485
Degenaar, N., & Wijnands, R. 2009, *A&A*, **495**, 547
Degenaar, N., & Wijnands, R. 2010, *A&A*, **524**, A69
D’Elia, V., Perri, M., Puccetti, S., et al. 2013, *A&A*, **551**, A142

- Eker, Z., Ak, N. F., Bilir, S., et al. 2008, *MNRAS*, **389**, 1722
- Evans, I. N., Primini, F. A., Glotfelty, K. J., et al. 2010, *ApJS*, **189**, 37
- Evans, P. A., Beardmore, A. P., Page, K. L., et al. 2009, *MNRAS*, **397**, 1177
- Evans, P. A., Osborne, J. P., Beardmore, A. P., et al. 2014, *ApJS*, **210**, 8
- Evans, P. A., Page, K. L., Beardmore, A. P., et al. 2023, *MNRAS*, **518**, 174
- Evans, P. A., Page, K. L., Osborne, J. P., et al. 2020, *ApJS*, **247**, 54
- Eyles-Ferris, R. A. J., Starling, R. L. C., O'Brien, P. T., & Evans, P. A. 2022, *MNRAS*, **515**, 4402
- Flesch, E. W. 2021, arXiv:2105.12985
- Gaskin, J. A., Swartz, D. A., Vikhlinin, A., et al. 2019, *JATIS*, **5**, 021001
- Gaia Collaboration, Brown, A. G. A., Vallenari, A., et al. 2021, *A&A*, **649**, A1
- Gehrels, N., Chincarini, G., Giommi, P., et al. 2004, *ApJ*, **611**, 1005
- Giacconi, R., Kellogg, E., Gorenstein, P., Gursky, H., & Tananbaum, H. 1971, *ApJL*, **165**, L27
- Ginsburg, A., Sipőcz, B. M., Brasseur, C. E., et al. 2019, *AJ*, **157**, 98
- Goia, I. M., Maccacaro, T., Schild, R. E., et al. 1990, *ApJS*, **72**, 567
- Goad, M. R., Tyler, L. G., Beardmore, A. P., et al. 2007, *A&A*, **476**, 1401
- Gobat, C., Yang, H., Kargaltsev, O., Hare, J., & Volkov, I. 2022, *RNAAS*, **6**, 163
- Gorgone, N. M., Kouveliotou, C., Negoro, H., et al. 2019, *ApJ*, **884**, 168
- Gorgone, N. M., Woudt, P. A., Buckley, D., et al. 2021, *ApJ*, **923**, 243
- Grimm, H. J., Gilfanov, M., & Sunyaev, R. 2002, *A&A*, **391**, 923
- Guillochon, J., Parrent, J., Kelley, L. Z., & Margutti, R. 2017, *ApJ*, **835**, 64
- Hasinger, G., Burg, R., Giacconi, R., et al. 1993, *A&A*, **275**, 1
- Hertz, P., & Grindlay, J. E. 1984, *ApJ*, **278**, 137
- Hu, C.-P., Begiçarslan, B., Güver, T., et al. 2020, *ApJ*, **902**, 1
- Israel, G. L., Rea, N., Mangano, V., et al. 2004, *ApJL*, **603**, L97
- Jackim, R., Szkody, P., Hazelton, B., & Benson, N. C. 2020, *RNAAS*, **4**, 219
- Jonker, P. G., Bassa, C. G., Nelemans, G., et al. 2011, *ApJS*, **194**, 18
- Kennea, J. A., Coe, M. J., Evans, P. A., Waters, J., & Jasko, R. E. 2018, *ApJ*, **868**, 47
- Kraft, R. P., Burrows, D. N., & Nousek, J. A. 1991, *ApJ*, **374**, 344
- Lacy, M., Baum, S. A., Chandler, C. J., et al. 2020, *PASP*, **132**, 035001
- Liu, Q. Z., van Paradijs, J., & van den Heuvel, E. P. J. 2006, *A&A*, **455**, 1165
- Liu, Q. Z., van Paradijs, J., & van den Heuvel, E. P. J. 2007, *A&A*, **469**, 807
- Luo, B., Brandt, W. N., Xue, Y. Q., et al. 2017, *ApJS*, **228**, 2
- Manchester, R. N., Hobbs, G. B., Teoh, A., & Hobbs, M. 2005, *AJ*, **129**, 1993
- Markwardt, C. B., Ransom, S., Woods, P., et al. 2003, *ATel*, **188**, 1
- Merc, J., Gális, R., & Wolf, M. 2019, *RNAAS*, **3**, 28
- Monet, D. G., Levine, S. E., Canzian, B., et al. 2003, *AJ*, **125**, 984
- Muno, M. P., Gaensler, B. M., Nechita, A., Miller, J. M., & Slane, P. O. 2008, *ApJ*, **680**, 639
- Muno, M. P., Lu, J. R., Baganoff, F. K., et al. 2005a, *ApJ*, **633**, 228
- Muno, M. P., Pfahl, E., Baganoff, F. K., et al. 2005b, *ApJL*, **622**, L113
- Mushotzky, R., Aird, J., Barger, A. J., et al. 2019, *BAAS*, **51**, 107
- Nandra, K., Barret, D., Barcons, X., et al. 2013, arXiv:1306.2307
- Nebot Gómez-Morán, A., Motch, C., Barcons, X., et al. 2013, *A&A*, **553**, A12
- Nebot Gómez-Morán, A., & Oskinova, L. M. 2018, *A&A*, **620**, A89
- Ng, C. Y., Slane, P. O., Gaensler, B. M., & Hughes, J. P. 2008, *ApJ*, **686**, 508
- Ochsenbein, F., Bauer, P., & Marcout, J. 2000, *A&AS*, **143**, 23
- O'Connor, B., Brink, J., Buckley, D. A. H., et al. 2023a, *ApJ*, **957**, 89
- O'Connor, B., Göğüş, E., Hare, J., et al. 2023b, *MNRAS*, **525**, 5015
- O'Connor, B., Göğüş, E., Huppenkothen, D., et al. 2022, *ApJ*, **927**, 139
- Olausen, S. A., & Kaspi, V. M. 2014, *ApJS*, **212**, 6
- Polidan, R. S., Pollard, G. S. G., Sanford, P. W., & Locke, M. C. 1978, *Natur*, **275**, 296
- Pretorius, M. L., Knigge, C., & Schwöpe, A. D. 2013, *MNRAS*, **432**, 570
- Revnivtsev, M., Sazonov, S., Churazov, E., et al. 2009, *Natur*, **458**, 1142
- Reynolds, M. T., Miller, J. M., Maitra, D., et al. 2013, *ATel*, **5200**, 1
- Rigoselli, M., Mereghetti, S., & Tresoldi, C. 2022, *MNRAS*, **509**, 1217
- Shaw, A. W., Heinke, C. O., Maccarone, T. J., et al. 2020, *MNRAS*, **492**, 4344
- Skrutskie, M. F., Cutri, R. M., Stiening, R., et al. 2006, *AJ*, **131**, 1163
- Sugizaki, M., Mitsuda, K., Kaneda, H., et al. 2001, *ApJS*, **134**, 77
- Tranin, H., Godet, O., Webb, N., & Primorac, D. 2022, *A&A*, **657**, A138
- Traulsen, I., Schwöpe, A. D., Lamer, G., et al. 2020, *A&A*, **641**, A137
- Ueda, Y., Takahashi, T., Inoue, H., et al. 1999, *ApJ*, **518**, 656
- Wang, Q. D., Gotthelf, E. V., & Lang, C. C. 2002, *Natur*, **415**, 148
- Webb, N. A., Coriat, M., Traulsen, I., et al. 2020, *A&A*, **641**, A136
- Wenger, M., Ochsenbein, F., Egret, D., et al. 2000, *A&AS*, **143**, 9
- Wijnands, R., in't Zand, J. J. M., Rupen, M., et al. 2006, *A&A*, **449**, 1117
- Willingale, R., Starling, R. L. C., Beardmore, A. P., Tanvir, N. R., & O'Brien, P. T. 2013, *MNRAS*, **431**, 394
- Yang, H., Hare, J., Kargaltsev, O., et al. 2022, *ApJ*, **941**, 104
- Yang, H., Hare, J., Volkov, I., & Kargaltsev, O. 2021, *RNAAS*, **5**, 102
- Zhang, W., Basu-Zych, A., Bautz, M., et al. 2022, *AAS/High Energy Astrophysics Division*, **54**, 108.45